Modeling ^{29}Si Chemical Shift in Crystalline and Amorphous Silicas

THESIS

Presented in Partial Fulfillment of the Requirements for

Graduation with Research Distinction in

Chemistry at The Ohio State University

By

Maxwell Christopher Venetos

* * * * *

The Ohio State University

2019

Thesis Committee:

Professor Noel Paul

Professor Philip J. Grandinetti, Adviser

Approved by

Adviser

Department of Chemistry

ABSTRACT

Using quantum-chemical calculations on a series of Q^4 silicate clusters, $(H_3SiO)_3$–Si–O–Si–$(OSiH_3)_3$, we examined the effects of changing Si-O-Si angle, Si-O distance, and O-Si-Si-O dihedral angle on the Si-29 isotropic chemical shift. We found a strong linear dependence of the chemical shift on the bridging oxygen s-character with variation in Si-O-Si angle. Furthermore, we propose a more accurate functional form for the mean bridging oxygen s-character in terms of the mean Si-O-Si angle. Through the use of principal component analysis we were able to obtain a reliable model predicting the Si-29 isotropic chemical shifts of Q^4 sites using strictly mean values of the Si-O-Si angle and Si-O distance, making model useful to amorphous and crystalline materials alike. This model is cross-validated (10-fold) using experimental Si-29 chemical shift data from 13 different crystalline silicas, with a total of 60 distinct Q^4 sites. Our chemical shift model not only gives a more accurate prediction of experiment of the Si-29 chemical shift of Q^4 sites, but it does so by requiring only two structural parameters, i.e., mean angle and distance. In contrast, previously existing models require 8 parameters, i.e., all four individual angles and four individual distances around a Q^4 site.

I dedicate this thesis to my parents, Brad and Laura Venetos.

ACKNOWLEDGMENTS

I would like to take this opportunity to thank everyone who has supported me on my academic journey throughout the years. My parents, Brad and Laura Venetos, have shown me support in all of my academic and personal endeavors and I would not have been able to make it this far without their love and support. I would also like to thank Dr. Timothy White for helping to start my path into scientific research and continuing to help me find new opportunities to develop as a scientist. I would like to give a special thanks to Dr. Deepansh Srivastava for his support and guidance throughout this project. He has shown a great amount of patience in helping me be successful in this thesis project and I am also grateful for him happily including me in all of his other projects. The rest of the Grandinetti lab also is worthy of mention, as all of this work could not have been done without their additional input. Finally, I would like to thank Dr. Philip J. Grandinetti for giving me the opportunity to conduct this research, but for also changing the path of my academic career. Dr. Grandinetti was my physical chemistry professor when I was unhappy with my pursuit of a chemical engineering degree. His passion and dedication to the class helped me develop an interest in physical and theoretical chemistry that motivated me to change my major and join his lab. His guidance and mentoring has affected me beyond the classroom as well by showing me how powerful keeping fundamentals in mind while conducting research is. Without the guidance and support of everyone in my life, I would not have been able to succeed in my goals as a researcher. I want to wish a very sincere thank you to everyone involved.

LIST OF FIGURES

Figure **Page**

LIST OF TABLES

Table **Page**

CHAPTER 1

Introduction

1.1 Nuclear Magnetic Resonance

Nuclear magnetic resonance (NMR) is a spectroscopic technique that detects the transitions of nuclear spins in a magnetic field. NMR spectroscopy may be used as a probe of the local electronic environment about a nuclei and the electronic environment of neighboring nuclei. Additionally, NMR can probe distance and geometry of neighboring nuclei through direct dipolar coupling of nuclear dipole moments.

1.1.1 The Magnetic Field at the Nucleus

Much like electrons, nuclei have an intrinsic spin angular momentum. The nuclear magnetic dipole moment vector, $\boldsymbol{\mu}$, and the spin angular momentum vector, $\boldsymbol{I}$, are closely linked to each other via a scalar constant

$$\boldsymbol{\mu} = \gamma \boldsymbol{I}, \tag{1.1}$$

where γ is the gyromagnetic ratio. When placed in a magnetic field, the magnetic dipole moment of the nuclei will begin to precess about the magnetic field as described by

$$\frac{d\boldsymbol{\mu}}{dt} = \gamma \boldsymbol{\mu} \times \boldsymbol{B}, \tag{1.2}$$

where $\boldsymbol{B}$ is the magnetic field vector experienced by the nuclei. It is tradition to take the z-component of the magnetic field vector in NMR. The precession of the magnetic dipole moment about the magnetic field is given by $\omega = -\gamma B_z$. When the external magnetic field, $B_{z,0}$, is uniform,

the nuclei of similar atoms will precess at the same frequencies. However, due to the electronic environments about each nuclei, there are subtle variations that change the magnetic field experienced at the nucleus. Because electrons are circulating electric charges, they produce an induced magnetic field, $B_{z,induced}$. The resulting local magnetic field felt by the nucleus is then a sum of the external and induced magnetic fields and becomes $B_{z,local} = B_{z,0} + B_{z,induced}$ which results in a new precession frequency given by

$$\omega = -\gamma B_{z,local}. \tag{1.3}$$

The subtle variations in the local magnetic fields are what allows NMR spectroscopy to be such a powerful probe of the electronic environments of a nuclei.

1.1.2 The NMR Signal

A magnetic dipole will tend to align itself with the external magnetic field, with a potential energy operator, $\hat{V}$, given by

$$\hat{V} = -\boldsymbol{\mu} \cdot \boldsymbol{B}. \tag{1.4}$$

It is traditional to take the magnetic field as the z-direction which simplifies equation 1.4 to

$$\hat{V} = -\mu_z B_z = -\gamma B_z \hat{I}_z. \tag{1.5}$$

When an external magnetic field is applied to a collection of nuclei, the magnetic dipole moments will begin to align with the magnetic field, where the spin dipole moments may take on only quantized energy values. For a spin 1/2 nucleus, these energy levels correspond to parallel or anti-parallel with the field. The build-up of nuclear magnetization in the z-direction when an external field is applied is given by

$$M_z(t) = M_{eq}(1 - e^{-(t-t_0)/T_1}), \tag{1.6}$$

where $M_z(t)$ is the net magnetization of the sample of nuclei at time t, M_{eq} is the equilibrium net magnetization of the sample of nuclei, and T_1 is known as the longitudinal relaxation time constant. This longitudinal spin magnetization, however, is nearly undetectable, and NMR measurements must instead measure magnetization precessing perpendicular to the external field. In order to do

so, an r.f. pulse is aplied to the sample of nuclei at thermal equilibrium which in effect shifts the direction of the net magnetization from the +z-direction to the -y-direction. After the magnetization is shifted to the -y-direction the magnetization will slowly precess and decay back to the +z-direction with a frequency

$$M_y = -M_{eq}\cos(\omega t)e^{-t/T_2} \tag{1.7}$$

in the y-direction, and

$$M_x = M_{eq}\sin(\omega t)e^{-t/T_2} \tag{1.8}$$

in the x-direction, where T_2 is the transverse relaxation time constant. In the NMR instrument, a coil is wrapped around the sample of nuclei in a direction perpendicular to the external magnetic field. Because we have an oscillating magnetic field from the transverse relaxation, we also generate an oscillating electric field. The oscillating electric field then generates a current in the coil which may be measured to give the magnetic resonance signal.

1.1.3 Nuclear Shielding and Chemical Shift

As alluded to earlier, the electronic environment about a nucleus in a magnetic field causes an induced magnetic field from the circulating electrons. This induced field is felt by the nucleus, and for diamagnetic substances, this induced field opposes the external field, leading to a shielding of the nucleus. The nuclear shielding, σ, may be described by a second rank tensor

$$\boldsymbol{\sigma} = \begin{pmatrix} \sigma_{xx} & \sigma_{xy} & \sigma_{xz} \\ \sigma_{yx} & \sigma_{yy} & \sigma_{yz} \\ \sigma_{zx} & \sigma_{zy} & \sigma_{zz} \end{pmatrix}. \tag{1.9}$$

Although the tensor is asymmetric, it is often treated as symmetric as a first approximation ($\sigma_{ij} = \sigma_{ji}$) because an NMR cannot measure the anti-symmetric components. Each unique bonding environment about a nucleus will yield a different nuclear shielding tensor. Because the magnetic fields produced by the circulating electrons change the net magnetic field at the nucleus, differences in the electron density due to the different bonding environments results in shielding or deshielding of the net magnetic field at the nucleus. The nuclear shielding tensor of a bare nucleus is $\boldsymbol{\sigma} = 0$,

meaning that any shielding will be positive and typically correlates to an increase in the electron density about the nucleus.

The shielding of the magnetic field may be calculated from the isotropic nuclear shielding, σ_{iso}, defined as

$$\sigma_{iso} = \frac{1}{3}(\sigma_{xx} + \sigma_{yy} + \sigma_{zz}) = \frac{1}{3}Tr\{\boldsymbol{\sigma}\}, \tag{1.10}$$

where the trace, $Tr\{\boldsymbol{\sigma}\}$, of the nuclear shielding tensor is the average of the eigenvalues of the principal axis. The magnetic field in terms of the nuclear shielding may be represented as $B = (1 - \sigma_{iso})B_0$. Therefore, the precession frequency of an NMR active nucleus may be described by

$$\omega = -\gamma(1 - \sigma_{iso})B_0. \tag{1.11}$$

Because the frequency of the nucleus' precession is dependent on the nuclear shielding, and therefore the bonding environment, the NMR shift is an excellent probe of the local environment about an atom.

Furthermore, the nuclear shielding tensor describes the shielding interactions in three dimensional space. The nuclear shielding tensor may be thought of as an ellipsoid in three dimensional space, and, to better illustrate this representation it is common to subtract the isotropic chemical shift from the diagonal components of the shielding tensor,

$$\lambda_{xx} = \sigma_{xx} - \sigma_{iso}, \tag{1.12}$$

$$\lambda_{yy} = \sigma_{yy} - \sigma_{iso}, \tag{1.13}$$

$$\lambda_{zz} = \sigma_{zz} - \sigma_{iso}, \tag{1.14}$$

where the λ_{ii} values may describe positive or negative deviations from a sphere. The orientation dependence of the deviation in three dimensional space is determined from the eigenvector of the particular eigenvalue of the tensor.

Measuring the magnetic field precisely is often difficult as the magnetic susceptibility of the sample and any fluctuations in the magnetic field must be taken into account. Instead, a more

convenient way to measure the chemical shift which is the difference between the sample and a reference shift. The isotropic chemical shift is defined as

$$\delta_{iso} = \frac{\omega_{iso} - \omega_{ref}}{\omega_{ref}} = \frac{\sigma_{ref} - \sigma_{iso}}{1 - \sigma_{ref}}, \tag{1.15}$$

where ω_{ref} and σ_{ref} indicate the Larmor frequency and nuclear shielding of reference compound respectively. The chemical shift is related to the nuclear shielding as $\sigma \approx -\delta$, therefore, increasing chemical shift corresponds to decreasing nuclear shielding. The chemical shift values, however, are difficult to relate to exact nuclear shielding values due to the need for an exact nuclear shielding reference.

1.2 NMR Crystallography

Traditionally, crystal structures have been solved using X-ray crystallography. While X-ray crystallography is a superb tool for accurate structural determination, it does have its limitations. Namely, single crystals which are nearly perfect are required for an accurate structure. Spatial or temporal disorder will cause uncertainty in the measurements. Additionally, amorphous materials cannot be adequately measured using X-ray diffraction methods as there is no periodic boundary conditions in the material. NMR spectroscopy, however, provides an excellent probe of the local structure where diffraction methods may struggle. NMR allows for the measurement of the structure in systems that are imperfect or amorphous. This advantage of NMR is due to it being a probe of molecular level and local interactions, whereas diffraction methods are long range and depend on repeating crystal cells. NMR is unlikely to replace diffraction methods but it does provide a strong complement to diffraction methods.

Isotropic chemical shift measurements have been used in solution phase NMR measurements for direct molecular level structural information and have similarly been used in solid state NMR. The isotropic chemical shifts in NMR crystallography may give information on the number of atom environments (the relative ratios of the different atom sites), and the atoms that are crystallographically relevant. Furthermore, the asymmetry and anisotropy of the nuclear shielding tensor may

also give detailed information on the electron density about the nuclei which can be correlated with diffraction measurement. Additionally, J-coupling measurements in solid state NMR may also give information on the atom connectivities in the crystal structure under study.

The pairing of NMR measurement with computational chemistry calculations has proven to be a powerful tool for the determination of the structure of materials. Computational calculations of shieldings, couplings, and quadropole coupling tensors have been increasingly more important in structural determination of crystalline materials. The repetition in periodic boundary conditions inherent in a crystal structure has been taken advantage of in the planewave-pseudopotential methodology used in CASTEP calculations. The pairing of these methods results in an iterative process in which a crystal structure is proposed, the NMR parameters calculated and compared to measurement, the crystal structure is adjusted, and this is repeated until the structure converges.

1.3 *Ab initio* Calculations of Nuclear Shielding Tensors

Many important values may be calculated by solving the wave equation using a given operator, such as the energy of a system using the Hamiltonian operator. While we can analytically solve the wave function for hydrogen like atoms, atoms with multiple electrons cannot be solved analytically and instead must be numerically solved. Computational chemistry has proven to be a useful tool to investigate chemical systems and correlate calculated trends with experimental observation. Computational chemistry has evolved with advances in computing power, and now for many systems *ab initio* methods are practical.

Ab initio methodologies approximate the wave function of a system using a basis set composed of a linear combination of functions, typically Gaussian functions. From the approximate wave function, different chemical parameters may be calculated, including NMR parameters. In quantum calculations, the nuclear shielding tensor is calculated as a perturbation to the overall Hamiltonian operator and is expressed as a mixed partial derivative of the energy

$$\sigma_i = \frac{\partial^2 E}{\partial B \partial m_i} \tag{1.16}$$

for a magnetic field, j, and an induced magnetic moment of atom i. Computational packages will typically solve for the nuclear shielding tensor using gauge independent atomic orbitals (GIAO) or continuouse set gauge transformations (CSGT) which differ in how the overal Hamiltonian operator is calculate with respect to the gauge origin.

CHAPTER 2

Computational Investigation of ^{29}Si Nuclear Shielding Tensors in Silicate Clusters

2.1 Introduction

Silicon-29 Nuclear Magnetic Resonance (NMR) spectroscopy has long play a critical role in structural studies of technologically important silica-based materials, ranging from zeolites to silicate glasses. Both the ^{29}Si isotropic chemical shift and J-couplings can play a key role as probes of atom geometry and connectivity.

While J couplings are a powerful probe of structure in liquid-state NMR spectroscopy, they have seen limited use in solid-state NMR studies [1–4]. This is because (1) the J-splittings are often minuscule compared to line widths in solid-state magic-angle spinning (MAS) NMR and, therefore, difficult to detect, and (2) our understanding of the relationships between J couplings and local structure had lagged behind other NMR probes of structure, such as chemical shifts and nuclear quadrupole couplings. An advance in solving the first problem was the NMR method called Phase-Incremented Echo Train Acquisition (PIETA), which not only removes the inhomogeneous broadenings obscuring J splittings in MAS spectra but also is a method for rapid and sensitive measurement of a 2D J-resolved spectrum [5] which correlates isotropic chemical shifts to J splittings. While both the INADEQUATE and J-resolved spectra give the same information of Si–Si connectivity, J-resolved NMR has added the advantages that (1) it provides a measure of the J coupling constant and (2) it employs single rather than double quantum excitation and, therefore, spectral intensities are quantitative. More recently, Srivastava et al. [4] have addressed the second

problem in discovering a robust analytical relationship for converting a geminal $^2J_{\text{Si–O–Si}}$ coupling into an inter-tetrahedral Si–O–Si angle.

In addition to J-couplings, ^{29}Si isotropic chemical shifts [6–10] are also a useful probe of the structure about the Si atom. There is, however, disagreement in the literature about whether and how to model the ^{29}Si isotropic chemical shift as depending only on Si–O–Si angle or to include Si–O distance. In this study, we examine analytical relationships between ^{29}Si isotropic chemical shift and local structure parameters in silica-based materials and develop a more broadly applicable analytical model. We use quantum-chemical calculations on a series of Q^4 silicate clusters to study the effects of local structure on the ^{29}Si isotropic chemical shift. The structure dependencies and correlations are modeled using strictly average values of the structural parameters so that the model may be used with amorphous and crystalline materials alike. The *ab initio* developed model is tested using crystalline data to determine its effectiveness.

Finally, with our combined models for chemical shift and J-coupling, we revisit the crystal structure refinement of zeolites Sigma-2 and ZSM-12 using the correlated ^{29}Si isotropic chemical shift and J couplings obtained from their 2D J-resolved PIETA spectra. To make the NMR spectra analysis more tractable we take on the experimental challenge of measuring the 2D J-resolved spectrum at ^{29}Si natural abundance levels, 4.7%, where, instead of the overlapping multiplet patterns [2] in ^{29}Si enriched samples, the J splittings appear as simpler overlapping doublet patterns arising from isolated ^{29}Si–O-^{29}Si linkages. Another advantage of natural abundance is that the homonuclear dipolar coupling between ^{29}Si is easily removed with MAS due to its inhomogeneous nature [11].

2.2 Methods

2.2.1 Nuclear Magnetic Resonance Spectroscopy

Pulse Sequence Under fast magic-angle spinning (MAS) all anisotropic frequency contributions are averaged to zero, and only the isotropic contributions to the frequency remain. We use symmetry pathways formalism [12] to describe the transition frequency of two weakly coupled spin $I = 1/2$

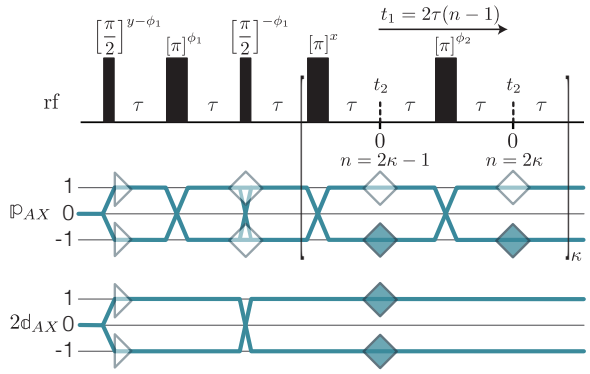

Figure 2.1: A graphical representation of the shifted-echo PIETA sequence and relevant symmetry pathways. Here $\kappa = 1..N$ and $n = 1...2N$ are echo counters where $2N$ is the number of echoes acquired.

nuclei in terms of the weakly coupled basis, $|m_A m_X\rangle$, as

$$\Omega_{AX} = -\omega_0 \sigma_{\text{iso},A}\, \mathbb{p}_A - \omega_0 \sigma_{\text{iso},X}\, \mathbb{p}_X - 2\pi J\, \mathbb{d}_{AX}. \tag{2.1}$$

Here, ω_0 is the Larmor frequency and $\sigma_{\text{iso},A}$, $\sigma_{\text{iso},X}$ are the isotropic nuclear shieldings of spin A and X respectively, and $\mathbb{p}_A$, $\mathbb{p}_X$, and $\mathbb{d}_{AX}$ are the spin transition symmetry functions

$$\begin{aligned} \mathbb{p}_A &= m_{A,j} - m_{A,i}, \\ \mathbb{p}_X &= m_{X,j} - m_{X,i}, \\ \mathbb{d}_{AX} &= m_{A,j} m_{X,j} - m_{A,i} m_{X,i}, \end{aligned} \tag{2.2}$$

where m_A and m_X are the quantized energy state quantum numbers and the subscript i and j denote the initial and the final energy state of the spin transition. The $\mathbb{p}_A$, $\mathbb{p}_X$, and $\mathbb{d}_{AX}$ functions reflect the symmetry of the frequency contributions under the orthogonal rotation subgroup, e.g., under a π pulse the $\mathbb{d}_{AX}$ spin transition symmetry function is invariant, whereas $\mathbb{p}_A$ and $\mathbb{p}_X$ spin transition symmetry functions change sign. In the case of two weakly coupled homonuclear nuclei, it is useful to define an additional transition symmetry function

$$\mathbb{p}_{AX} = \mathbb{p}_A + \mathbb{p}_X. \tag{2.3}$$

In the case of weak ^2J coupling between dilute spin-1/2 pairs under fast magic-angle spinning (MAS), the shifted-echo Phase Incremented Echo Train Acquisition (SE-PIETA) pulse sequence,

shown in Fig. 2.1, separates and correlates the third frequency term in Eq. (2.1), the weak J coupling, with the isotropic nuclear shielding shifts of first and second terms in Eq. (2.1). From hereafter, we will use the isotropic chemical shift, δ, instead of isotropic nuclear shielding where the conversion between the two is given by

$$\delta = \frac{\sigma_{\text{reference}} - \sigma_{\text{isotropic}}}{1 - \sigma_{\text{reference}}}, \tag{2.4}$$

where $\sigma_{\text{reference}}$ is the isotropic nuclear shielding of a reference compound.

The shifted-echo PIETA pulse sequence eliminates a signal artifact present in the original PIETA experiment for J-resolved spectroscopy which arises from an inability to acquire a full echo for $t_1 = 0$ ($n = 1$) cross-section. Using the shifted-echo approach [13], in the case of 2D J-resolved spectroscopy, requires a simultaneous echo of both $\mathbb{p}_{AX}$ and $\mathbb{d}_{AX}$ transition symmetries at $t_1 = 0$ cross-section. It is well known [14–16] that such a simultaneous echo, in the case of two weakly coupling nuclei, can be generated with the sequence

$$\text{equilibrate} - \frac{\pi}{2} - \tau - \pi - \tau - \frac{\pi}{2} - \tau - \pi - \tau \rightarrow \bullet \tag{2.5}$$

The first $\pi/2$ pulse on a system of two weakly coupled spin 1/2 nuclei excites all eight single quantum transitions which then evolves for a period τ. Next, the π pulse converts the transition $|m_{A,j}, m_{X,j}\rangle \langle m_{A,i}, m_{X,i}|$ entirely into the transition $|-m_{A,j}, -m_{X,j}\rangle \langle -m_{A,i}, -m_{X,i}|$ leaving the number of transition pathways after the π pulse at eight. By the end of the second τ period, all chemical shift evolution phase on these eight transition pathways refocus into a $\mathbb{p}_{AX}$ echo as indicated in Fig. 2.1. At this point, these eight transition pathways can be divided into two sets of four with the first set having the same negative J (or $\mathbb{d}_{AX}$) evolution:

$$\underbrace{A_2^* \overset{\pi}{\rightarrow} A_1, \quad X_2^* \overset{\pi}{\rightarrow} X_1,}_{\begin{array}{rcl}\mathbb{p}_{AX} & = & +1 \rightarrow -1 \\ 2\mathbb{d}_{AX} & = & -1 \rightarrow -1\end{array}} \quad \underbrace{A_1 \overset{\pi}{\rightarrow} A_2^*, \quad X_1 \overset{\pi}{\rightarrow} X_2^*,}_{\begin{array}{rcl}\mathbb{p}_{AX} & = & -1 \rightarrow +1 \\ 2\mathbb{d}_{AX} & = & -1 \rightarrow -1\end{array}} \tag{2.6}$$

and the other set having the same positive J (or $\mathbb{d}_{AX}$) evolution:

$$\underbrace{A_1^* \overset{\pi}{\rightarrow} A_2, \quad X_1^* \overset{\pi}{\rightarrow} X_2,}_{\begin{array}{rcl}\mathbb{p}_{AX} & = & +1 \rightarrow -1 \\ 2\mathbb{d}_{AX} & = & +1 \rightarrow +1\end{array}} \quad \underbrace{A_2 \overset{\pi}{\rightarrow} A_1^*, \quad X_2 \overset{\pi}{\rightarrow} X_1^*}_{\begin{array}{rcl}\mathbb{p}_{AX} & = & -1 \rightarrow +1 \\ 2\mathbb{d}_{AX} & = & +1 \rightarrow +1\end{array}}. \tag{2.7}$$

The second $\pi/2$ pulse has the similar effect as in a solid echo experiment [17], which is to transfer coherence only between single quantum transitions with opposite signs of $\mathbb{d}_{AX}$. As the $\mathbb{d}_{AX}$ values of transitions remain invariant under the second π pulse while the $\mathbb{p}_{AX}$ symmetries refocus again into an echo, there will be a simultaneous echo of both $\mathbb{p}_{AX}$ and $\mathbb{d}_{AX}$ symmetries at the end of the fourth τ period as shown in Fig. 2.1. It is also worth noting that with perfect $\pi/2$ and π rotations the transition pathways in two weakly coupled nuclei generate a simultaneous echo at $t_1 = 0$ with no loss of intensity to other transition pathways. After the formation of the simultaneous echo, the chemical shift evolution can be continually refocused by a train of π pulses into echoes whose modulation by J evolution provides the desired frequency separation.

2.2.2 Experimental

The J-couplings were measured for two samples, Sigma-2 and ZSM-12, using the SE-PIETA sequence with t_1 interleaving. The measurements were performed on the Bruker Avance III HD 400 MHz NMR spectrometer operating at 9.4 T with ^{29}Si and ^{1}H Larmor frequency of 79.56935 MHz and 400.5989344 MHz, respectively, using a 4 mm Bruker MAS probe. The magic angle was calibrated using STMAS measurement on Na_2SO_4. This method gives a better calibration of the magic angle, within 0.001°, that the traditional KBr spinning sidebands method. The sample spinning speed was set at 12.5 kHz $\pm$ 1 Hz for both measurements. The ^{29}Si chemical shift was referenced with respect to TMS at 0 ppm.

Sigma-2: An additional ^{1}H to ^{29}Si cross-polarization was performed prior to the J-coupling measurements. The ^{1}H polarization was excited using an rf pulse of field strength 125 kHz and a t_{90° of 2 μs. This polarization was then transferred to ^{29}Si using the simultaneous spin lock rf pulses on each nucleus for a contact period of 9 ms. During the contact period, the rf field strength for ^{29}Si was set to 8.7 kHz while the rf field strength for ^{1}H was amplitude modulated using a linear 100% - 90% ramp with the maximum rf field strength of 19.14 kHz. During the echo train acquisition, the rf field strength on ^{29}Si was set to 117.65 kHz with a t_{90° and t_{180° of 2.125 μs and 4.25 μs, respectively. A low power ($\sim$ 51 mW, rf field strength $\sim$ 2.5 kHz) ^{1}H-^{29}Si constant

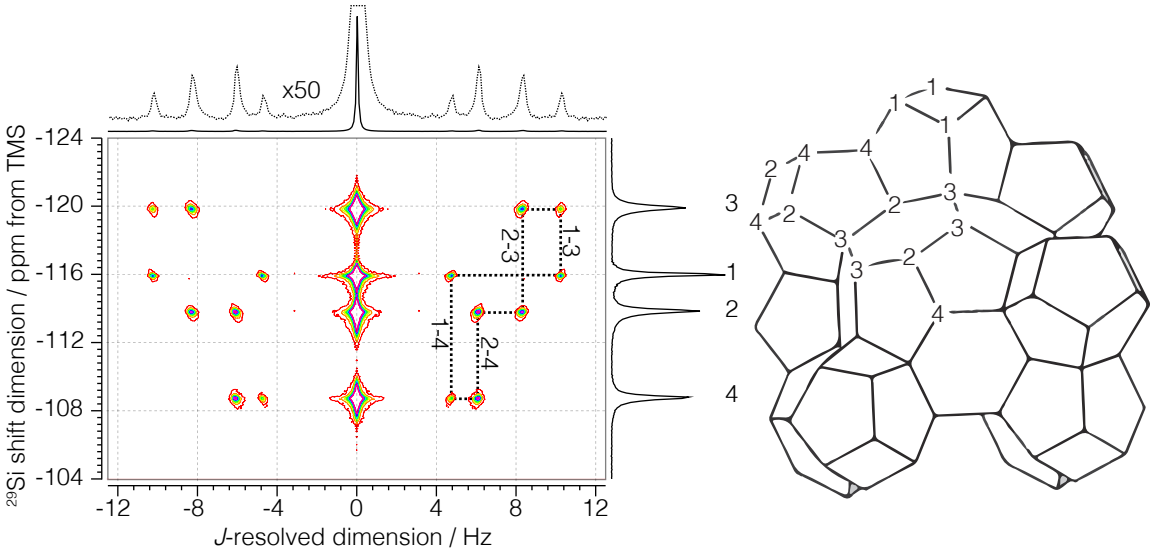

Figure 2.2: Experimental 2D J-resolved ^{29}Si NMR spectrum of siliceous zeolite Sigma-2.

decoupling was applied during the measurement using spinal16_12 decoupling scheme. The sample temperature was maintained at 25°C and the recycle delay was set to 5 s. The ^{1}H relaxation time, T_1, was measured to be 2.08 ± 0.05s.

The echoes along the t_2 dimension were acquired for 159.36 ms at a sampling rate of 311.25 μs/point for 512 complex points. A total of 288 echoes were collected with four ($M = 4$) t_1 interleaving steps of 72 echoes each. The inter-echo period, 2τ, was set to 160 ms. The phase increments on the first, ϕ_1, and the second, ϕ_2, phase dimensions were set to $\pi/6$ and $\pi/40$ with 12 and 80 phase points, respectively. The total experiment time with a single SE-PIETA measurement was approximately 17.92 hours.

ZSM-12: The ^{29}Si relaxation time, T_1, was measured to be 12 ± 2 s, however, only 20 s of recovery time was allowed per scan. For this reason, four dummy scans were added before the start of the experiment to reach a steady non-equilibrium density state. The rf field strength on ^{29}Si was set to 96.15 kHz with a t_{90° and t_{180° of 2.6 μs and 5.2 μs, respectively. A total of 288 echoes were acquired with three (M=3) t_1 interleaving steps of 96 echoes each. Each echo was acquired with 384 complex data points sampled at every 311.25 μs with an echo acquisition window of 119.52 ms along

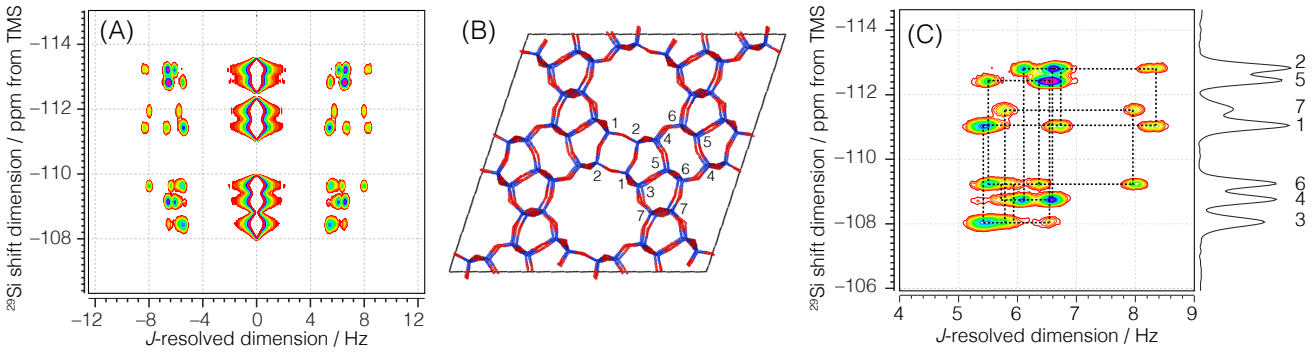

Figure 2.3: Experimental 2D J-resolved ^{29}Si NMR spectrum of siliceous zeolite ZSM-12.

the t_2 dimension. The inter-echo period, 2τ, was set to 120 ms. The phase increments on the first, ϕ_1, and the second, ϕ_2, phase dimensions were set to $\pi/6$ and $\pi/50$ with 12 and 100 phase points, respectively. With this setup, the time for a single SE-PIETA measurement was approximately 31.8 hours. The signal was averaged over 15 SE-PIETA measurements spanning over approximately 20 days. The sample temperature was maintained at 29°C throughout the experiment.

The 2D J-resolved spectra in Figs. 2.2 and 2.3 were analyzed to determine ^{29}Si isotropic chemical shifts, $^2J_{\text{Si–O–Si}}$ couplings, and connectivity. To interpret a J-resolved spectra, each ^{29}Si site is on the abscissa (horizontal) and couplings between Si sites are on the ordinate (vertical). For example, in Fig. 2.2 it can be seen that Si3 at -119.7 ppm has two peaks on its ordinate and is thus coupled to two different Si sites. Similarly, Si1, Si2, and Si4 at -115.8, -113.6, and -108.5 ppm respectively are also each coupled to two Si sites. Si1 and Si3 and Si2 and Si3 have peaks on the same abscissa and thus Si3 is coupled Si1 and Si2 with J-couplings of 20.5 and 16.7 Hz respectively. In the same manner, Si1 is additionally coupled to Si4, and Si2 is additionally coupled to Si4. These couplings in the chemical shift versus J-resolved dimension give the connectivities shown in Fig. 2.2. The results of spectral processing and analysis are summarized in Table 2.1.

2.2.3 Computational

All *ab initio* calculations were carried out using Gaussian'16 [18]. The ^{29}Si nuclear shielding tensors and $^2J_{\text{Si–O–Si}}$ couplings were calculated using DFT with B3LYP [19] functional on a small O

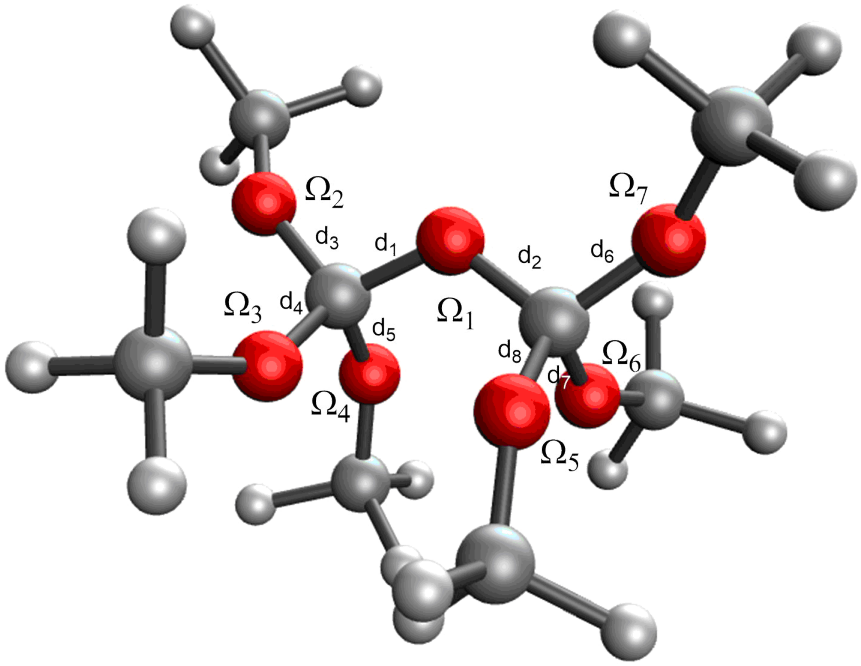

Figure 2.4: Oxygen centered SiH_3 terminated cluster, $(H_3SiO)_3$–Si–O–Si–$(OSiH_3)_3$.

Sigma-2			
^{29}Si Index	δ_{iso}/ppm	^{29}Si Pairs	J/Hz
1	-115.8	1-3	20.5
2	-113.6	1-4	9.3
3	-119.7	2-3	16.7
4	-108.5	2-4	12.2
ZSM-12			
^{29}Si Index	δ_{iso}/ppm	^{29}Si Pairs	J/Hz
1	-111.1	1-2	13.4, 16.6
2	-112.9	1-3	10.6
3	-108.1	2-4	12.1, 13.2
4	-108.7	3-5	13.2
5	-112.5	3-7	11.6
6	-109.3	4-5	13.2
7	-111.6	4-6	11.2
		5-6	10.8, 12.6
		6-7	15.9

Table 2.1: ^{29}Si isotropic chemical shifts and J couplings determined from the shifted-echo PIETA experiments for Sigma-2 and ZSM-12 shown in figures 2.2 and 2.3 respectively.

centered SiH_3 terminated cluster, $(H_3SiO)_3$–Si–O–Si–$(OSiH_3)_3$ as shown in Fig. 2.4. A tetrahedron angle ∠O-Si–O = 109.5° was imposed about Si atoms in all calculations.

A locally dense basis set was implemented on this cluster, as suggested by Cadars *et al.* [3], for accurate ^{29}Si nuclear shielding tensor and $^2J_{Si–O–Si}$ coupling calculations. This follows an implementation of cc-PV5Z basis set on the two central Si, 6-31++G basis set on all H, and 6-31++G* basis set on all O and remaining Si. Single point GIAO [20] NMR(spinspin) and NBO version 3.1 [21] calculations were run with tight self consistent field convergence criteria and *'fine'* integration grid.

Systematic structural variations of the cluster were performed to investigate the ^{29}Si nuclear shielding dependence on and correlations between the Si–O–Si bond angles, Ω_i, and Si–O bond distances, d_i, about a Si atom. These investigations were done with three series of calculations:

Series 1 A uniform two-dimensional grid was created by varying all seven Ω_i simultaneously and identically from 135 ° to 165 ° in 5 ° increments for each fixed bond distance, and each bond

Series	$\langle\Omega\rangle(^\circ)$	$\langle d_i\rangle$ (Å)
1	135 – 165	1.54 – 1.64
2	139.5 – 154.5	1.54 – 1.64
3	139.5 – 154.5	1.585 – 1.61

Table 2.2: Summary of average angle and average bond distance range of each series.

distance, d_{ij}, varied simultaneously and identically from 1.54 Å to 1.64 Å in 0.01 Å increments for each fixed angle.

Series 2 A second series of calculations was performed, which is an extension of the calculations performed by Srivastava *et al.* [4]. A uniform two-dimensional grid was created by varying the central Si–O–Si bond angle, Ω_0, from 120 ° to 180 ° in 10 ° increments while the remaining Si–O–Si bond angles, $\Omega_{i\neq 0}$, were held at 146 °. The Si–O bond distances, d_{ij}, were simultaneously and identically varied from 1.54 Å to 1.64 Å in 0.01 Å increments for each central angle, Ω_0.

Series 3 In a third series of calculations a uniform two-dimensional grid was created for an asymmetric linkage by varying Ω_0 from 120 ° to 180 ° in 10 ° increments and the d_{12} bond distance was varied from 1.54 Å to 1.64 Å in 0.01 Å increments for each angle. The remaining $\Omega_{i\neq 0}$ and $d_{ij\neq 12}$ bond distances were held at 146 ° and 1.6 Å, respectively.

A summary of the average Si–O–Si bond angle and Si–O bond distance range is summarized in the Table 2.2.

Natural Bond Order Analysis

The natural bond orbital (NBO) and natural localized molecular orbital (NLMO) analysis were performed to verify that the clusters resemble Q^4 silicates as suggested by Tossell *et al.* [22]. From the NBO and NLMO analyses in clusters with short Si–O bond lengths and large Si–O–Si bond angles, a bond order of 3 would form between a Si and O bond in the cluster delocalized over

Cluster Series	$\langle\Omega\rangle$ / °	$\langle d_i\rangle$ / Å
1	145	1.54
1	150	1.54
1	155	1.54
1	160	1.54
1	165	1.54
1	155	1.55
1	160	1.55
1	165	1.55
1	165	1.56
2	149.5	1.54
2	152	1.54
2	154.5	1.54
2	147	1.55
2	149.5	1.55
2	152	1.55
2	154.6	1.55
2	149.5	1.56
2	152	1.56
2	154.5	1.56
3	152	1.585
3	154.5	1.585

Table 2.3: Series number, average angle, and average bond distance of clusters removed after NBO and NLMO analysis.

all Si–O bonds in the cluster. As described by Cruickshank [23] and Oldfield *et al.* [7, 24], high bond orders are due to (d-p)π-bonding and are indicative of unpolymerized silica rather than a fully polymerized Q^4 site. Although the clusters are not fully unpolymerized, the high bond orders found in some clusters indicates bonding instances more closely resembling the unpolymerized Si sites than the Q^4 sites. Because these bonds are not representative of Q^4 sites, clusters exhibiting these high bond orders were not considered for analysis. Table 2.3 shows the clusters removed from consideration due to the occurrence of bond orders of 3 between a Si–O bond.

2.3 Results

2.3.1 Nuclear shielding dependence on local structure

Si–O–Si bond angle

The ^{29}Si isotropic nuclear shielding, σ_G, from series 1 cluster Gaussian'16 calculations are shown in Fig. 2.5A and 2.5B. Figure 2.5A highlights the dependence of ^{29}Si isotropic nuclear shielding, σ_G, on the average Si–O–Si bond angle, $\langle\Omega\rangle$, in the range of $\langle\Omega\rangle \in [135°, 165°]$, where,

$$\langle\Omega\rangle = \frac{1}{4}\sum_{i=1}^{4}\Omega_i \tag{2.8}$$

for each Si–O bond about a Si atom. The dependence of σ_G on $\langle\Omega\rangle$ is shown for fixed Si–O bond distances and a constant O–Si–Si–O dihedral angle of 0 °. It can be seen that the nuclear shielding has an approximately linear response to increasing average Si–O–Si bond angle which deviates from linearity slightly at mean angles greater than 150 °. Over the range of Si–O–Si angles analyzed, the nuclear shielding varies by 20 to 30 ppm for a given bond length. It is clear that the mean Si–O–Si bond angle is the dominant factor in determining the ^{29}Si nuclear shielding for the range of geometry parameters analyzed.

Si–O Bond Distance

Shown in Fig. 2.5B is the dependence of the Gaussian calculated ^{29}Si nuclear shielding, σ_G, on the average Si–O bond distance, $\langle d_i\rangle$, in the range $\langle d_i\rangle \in [1.54\text{Å}, 1.64\text{Å}]$, where

$$\langle d_i\rangle = \frac{1}{4}\sum_{i=1}^{4} d_i \tag{2.9}$$

for each Si–O bond about a Si atom. The dependence of σ_G on $\langle d_i\rangle$ is shown for constant average Si–O–Si bond angle and an O–Si–Si–O dihedral angle of 0°. The calculated σ_G values show a small nonlinear increase in shielding with an increase in average Si–O bond distance. Although the effect from the bond distance is small, it is non-negligible, owing a variation of about 5-7 ppm for a given average Si–O–Si bond angle. The average Si–O bond distance is found to give a minor contribution to the ^{29}Si nuclear shielding and must also be included in the model.

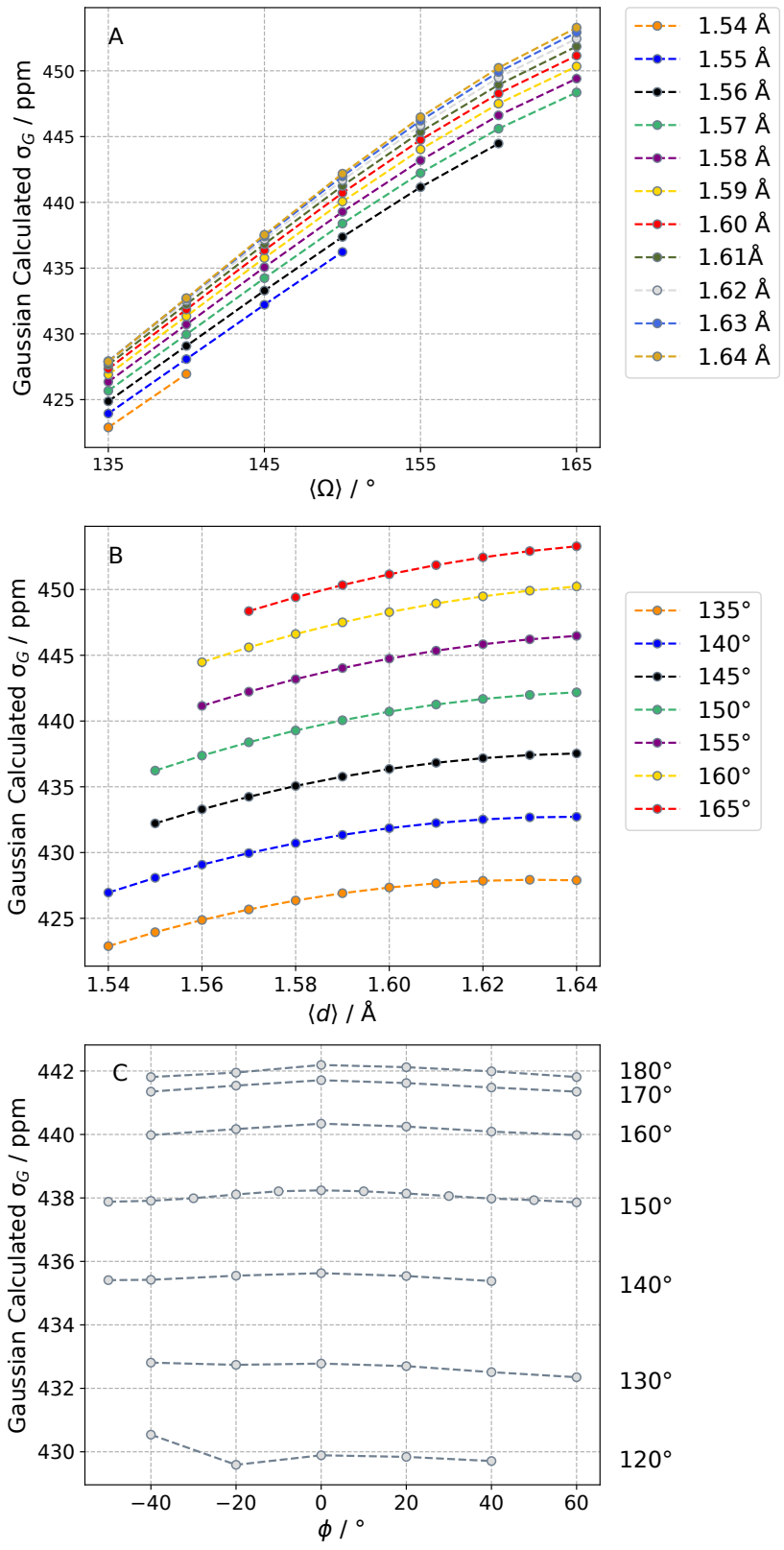

Figure 2.5: Dependence of ^{29}Si nuclear shielding on A) Si–O–Si angle, B) Si–O distance, and C) O–Si–Si–O dihedral angle for series 1 cluster calculations.

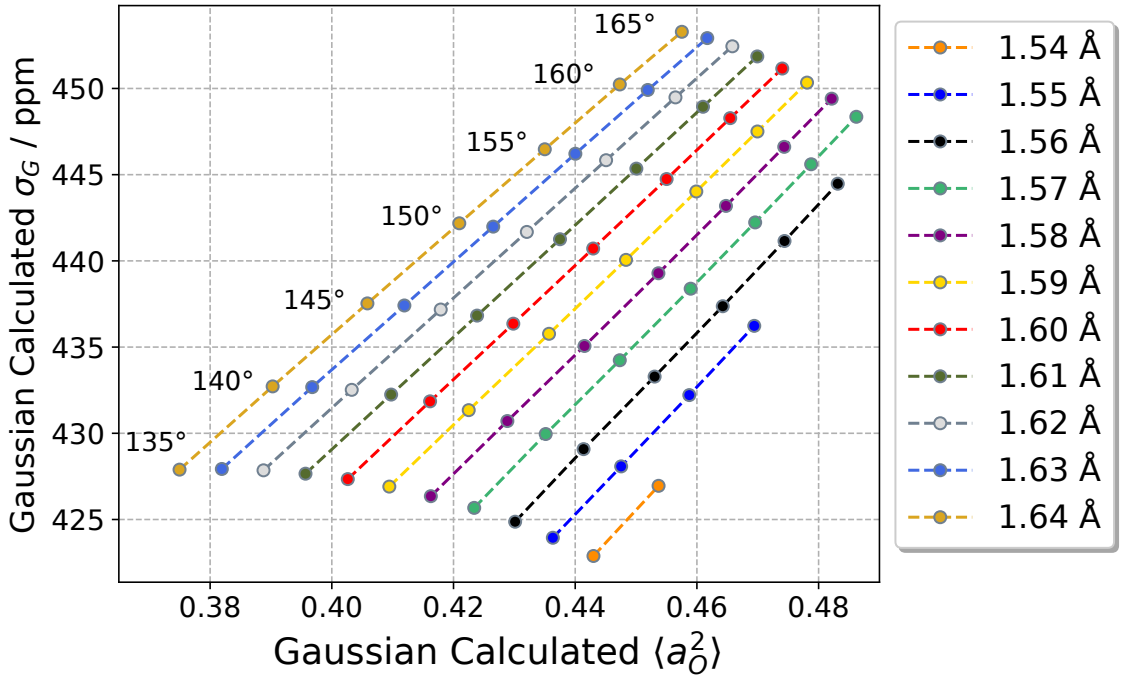

Figure 2.6: Dependence of ^{29}Si nuclear shielding on bridging oxygen s-character for different fixed Si–O distances.

O–Si–Si–O Dihedral Angle

The raw data from calculations for Fig. 2B of Srivastava *et al.* [4] were further analyzed to examine the effects of O–Si–Si–O dihedral angle, ϕ on σ_G. The clusters used had $\langle \Omega \rangle \in [120°, 180°]$, and a $\langle d_i \rangle$ of 1.60 Å. The angle ϕ was varied from -50 ° to 60 ° for each $\langle \Omega \rangle$, and the results are shown in Fig. 2.5C. ϕ has little to no affect on σ_G. The largest difference seen in the $\langle \Omega \rangle = 120°$ cluster is less than 1 ppm and the remaining variations are all less than 0.5 ppm. Because of the very small variations of the nuclear shielding in the data, we assume that variations of ^{29}Si nuclear shielding due to ϕ can be neglected, and will not be considered in our modeling.

2.3.2 29Si nuclear shielding model for Q4

Oxygen s-character is well documented as having a strong correlation to ^{29}Si chemical shift [6, 7]. The plot in Fig. 2.6 shows, for a fixed Si–O distance, a clear linear correlation between the

Gaussian'16-calculated shielding, σ_G and mean s-character, $\langle a_O^2 \rangle$, of the four bridging oxygen of an SiO_4. This may be modeled as

$$\sigma\left(\langle a_O^2\rangle, \langle d_i\rangle\right) = m(\langle d_i\rangle)\,\langle a_O^2\rangle + b(\langle d_i\rangle), \tag{2.10}$$

where one can go further and obtain functional forms for $m(\langle d_i\rangle)$ and $b(\langle d_i\rangle)$ by analyzing the dependence on bond length. Both functional forms for $m(\langle d_i\rangle)$ and $b(\langle d_i\rangle)$ were found to fit well to quadratic functions, as shown in Fig. 2.7. Quadratic functional forms were substituted back into Eq. (2.10) to give

$$\sigma\left(\langle a_O^2\rangle, \langle d_i\rangle\right) = (\alpha_d\langle d_i\rangle^2 + \beta_d\langle d_i\rangle + \gamma_d)\,\langle a_O^2\rangle + (\epsilon_d\langle d_i\rangle^2 + \zeta_d\langle d_i\rangle + \eta_d). \tag{2.11}$$

The coefficients $\alpha_d,\ \beta_d,\ \gamma_d,\ \epsilon_d,\ \zeta_d$ and η_d were then found via a least-squares linear regression.

Eq. (2.11) gives an excellent prediction of the nuclear shielding, as shown in Fig. 2.8, an analytical model requiring the mean oxygen s-character, however, has limited utility in an NMR structure determination because mean oxygen s-character is not a experimentally observable. A more practical model is needed which replaces the average oxygen s-character dependence with its dependence on structural coordinates.

Engelhardt and Radeglia [6] used a popular model for the oxygen s-character, developed from approximate molecular orbital theory, which describes the s-character as a function of Si–O–Si bond angle

$$a_O^2 \approx \rho(\Omega) = \frac{\cos(\Omega)}{(\cos(\Omega) - 1)}. \tag{2.12}$$

and found an approximately linear relationship between the average $\rho(\Omega_i)$ around the Si atom,

$$\langle\rho(\Omega_i)\rangle = \frac{1}{4}\sum_{i=1}^{4}\frac{\cos(\Omega_i)}{(\cos(\Omega_i) - 1)} \tag{2.13}$$

and the ^{29}Si chemical shift given by

$$\delta_E(\Omega_i) = -a_E\langle\rho(\Omega_i)\rangle + b_E. \tag{2.14}$$

When plotting $\langle\rho(\Omega_i)\rangle$ to $\langle a_O^2\rangle$, however, we still find a significant degree of curvature in the correlation, as shown in Fig. 2.9A. This curvature in the $\langle\rho(\Omega_i)\rangle$ model carries over into the nuclear

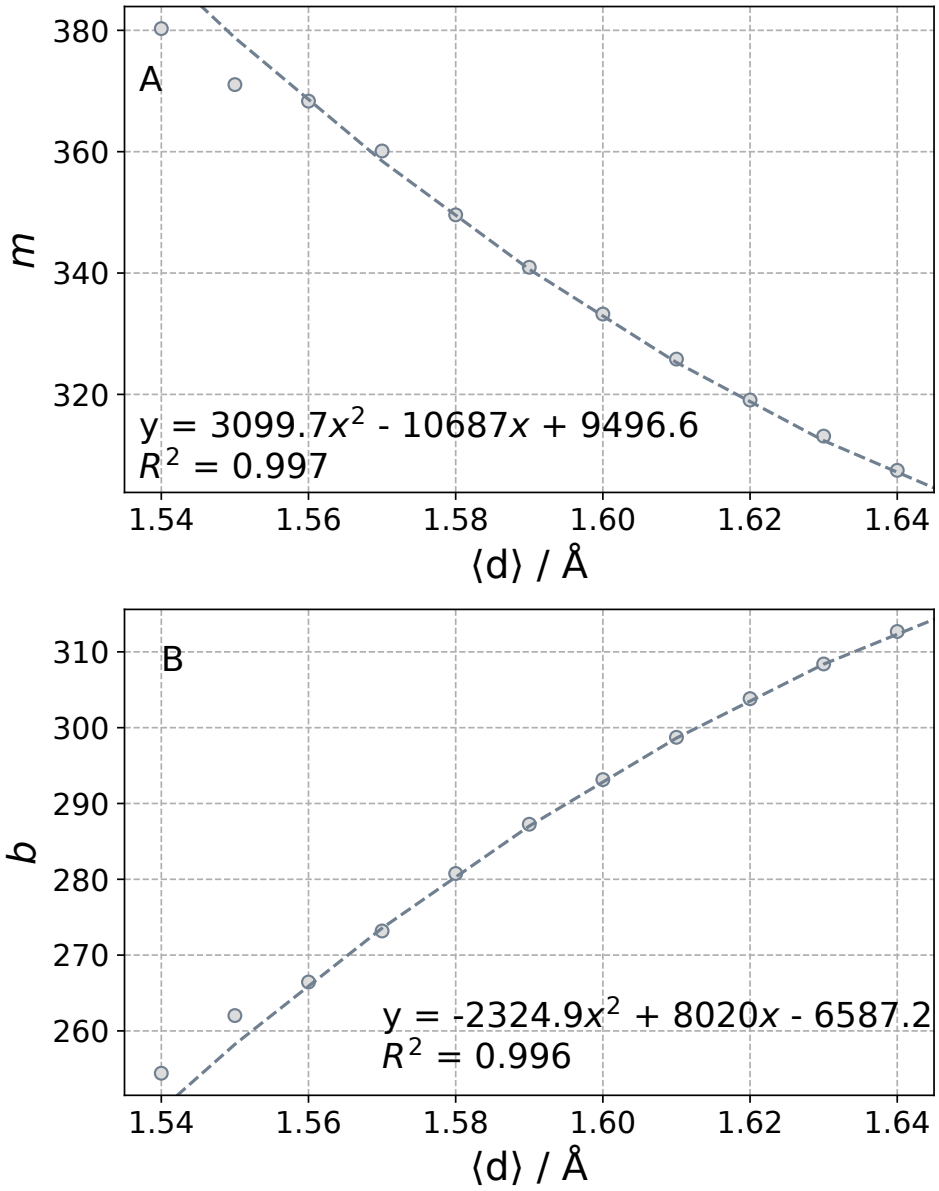

Figure 2.7: The fit of quadratic equations to determine the functional forms of $m(\langle d_i \rangle)$ and $b(\langle d_i \rangle)$.

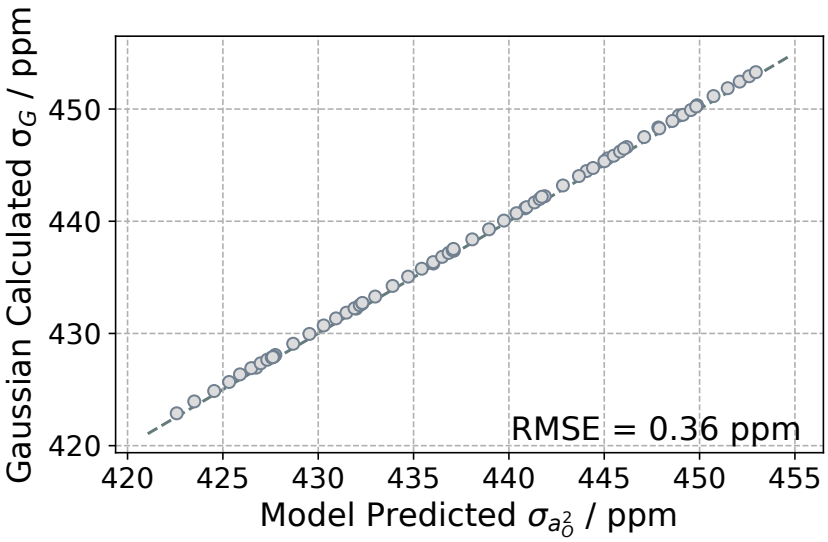

Figure 2.8: The predicted nuclear shieldings from equation the mean oxygen s-character model versus the nuclear shieldings observed from the cluster calculations around the line y = x.

shielding model, as shown in Fig. 2.10A, making it less suitable model for the oxygen s-character and for use in Eq. (2.10).

Furthermore, the Engelhardt and Radeglia chemical shift model also shows a significant vertical spread of nuclear shieldings as was expected due to the absence of any bond distance dependence in the model. In a study of ^{29}Si chemical shifts in zeolite materials Davis *et al.* found that better agreement could be obtained by weighting the ρ term by the corresponding Si–O bond distance, as illustrated in Fig. 2.11. Davis *et al.* proposed the following model

$$\delta_D(\Omega_i) = -a_D \langle d_i \ \rho(\Omega_i) \rangle + b_D \tag{2.15}$$

where,

$$\langle d_i \ \rho(\Omega_i) \rangle = \frac{1}{4} \sum_{n=1}^{4} d_i \frac{\cos(\Omega_i)}{(\cos(\Omega_i) - 1)}.$$

While Eq. (2.15) reduces the vertical spread of ^{29}Si chemical shift, there is still some residual spread due to the distance dependence inside the correlation. As seen in Fig. 2.5B, the nuclear shielding shows a non-linear response to varying bond distance and therefore an improved description is required.

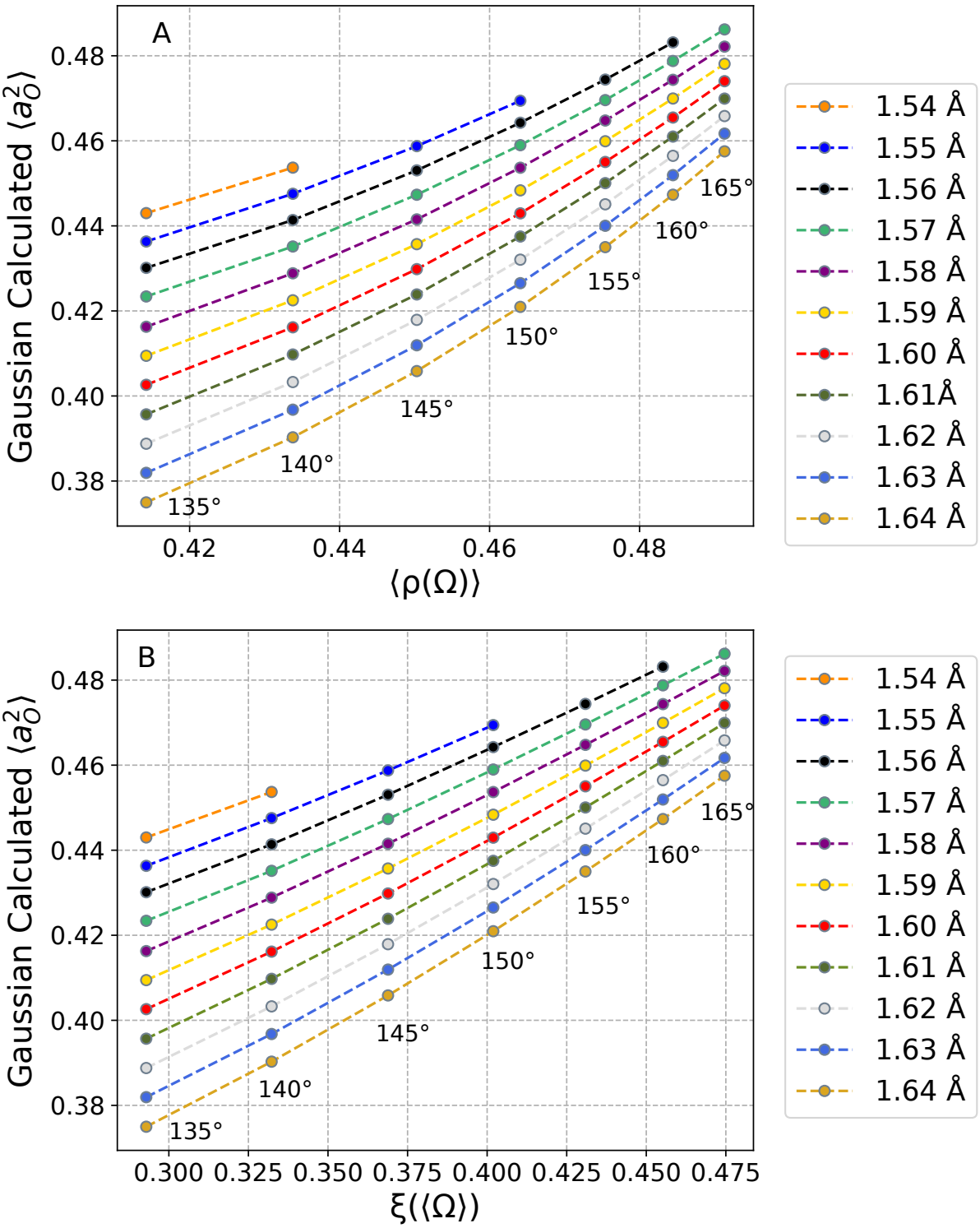

Figure 2.9: The oxygen s-character predicted by (A) the ρ and (B) the ξ model versus the observed s-character.

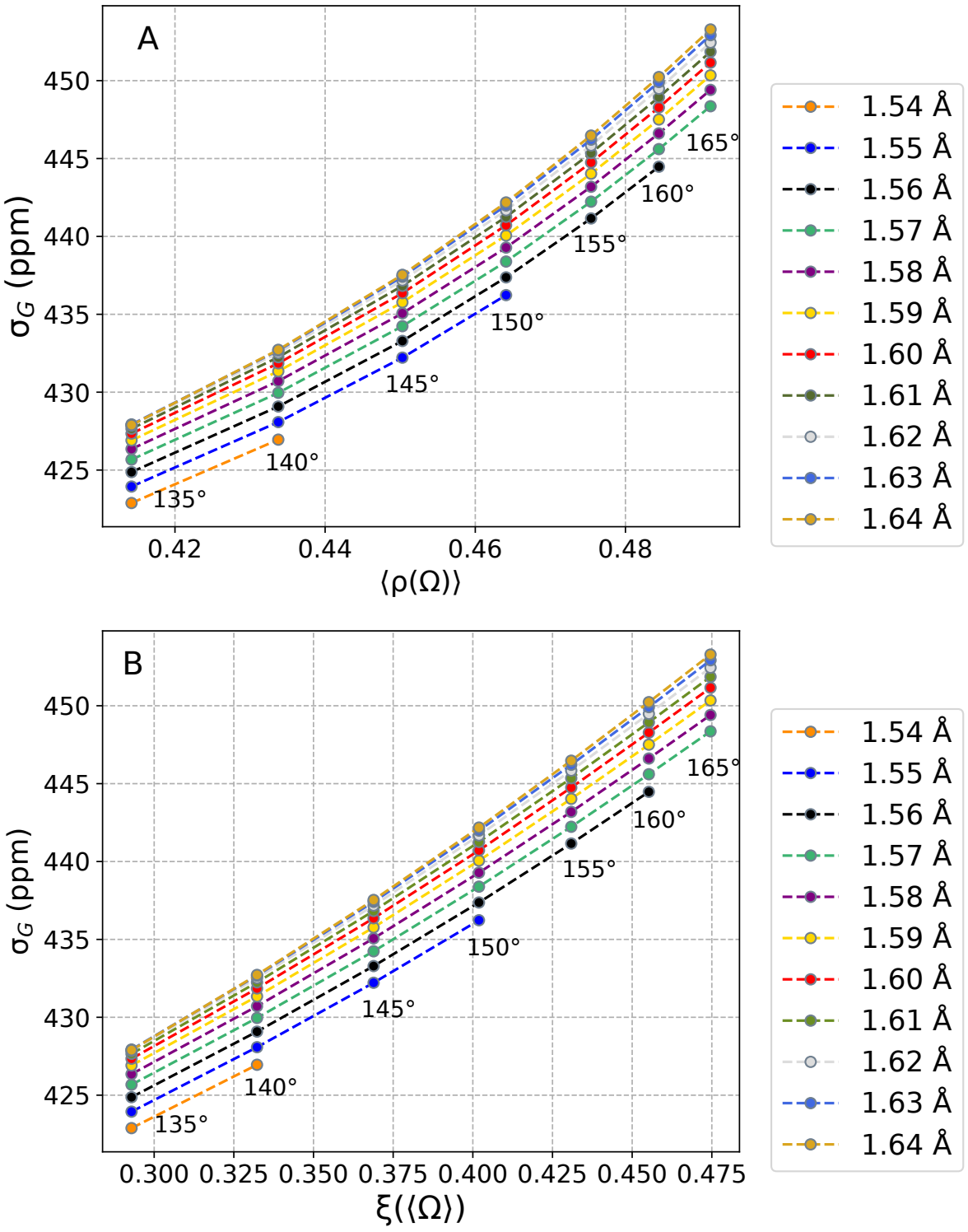

Figure 2.10: (A) The ρ model versus the observed nuclear shieldings. (B) The Davis *et al.* model versus the observed nuclear shiledings and C) the ξ model versus the observed nuclear shieldings.

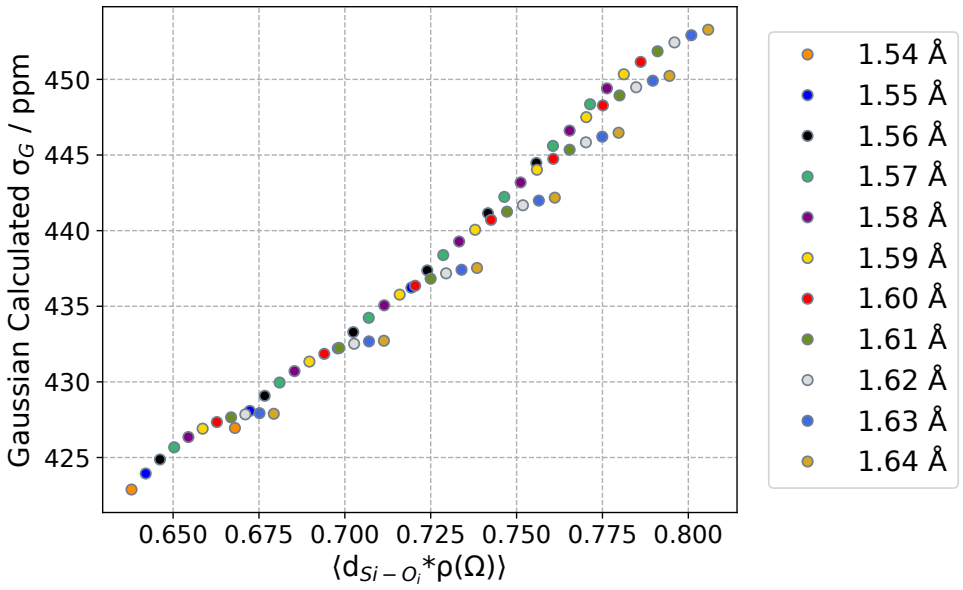

Figure 2.11: The oxygen s-character predicted by the (A) ρ and (B) the ξ model versus the observed s-character.

The model function we propose is a more practical description of the four oxygen s-character mean, $\langle a_O^2 \rangle$, as a function of the four angle mean, $\langle \Omega \rangle$, and the four distance mean, $\langle d_i \rangle$ of the Q^4 site. Additionally, this model function outperforms the Davis *et al.* model in terms of both accuracy and simplicity. In this effort we model the oxygen s-character as

$$\xi(\langle \Omega \rangle) = \frac{\cos^2(\langle \Omega \rangle)}{1 - \cos(\langle \Omega \rangle)}, \tag{2.16}$$

where $\langle \Omega \rangle$ is the average of the four Si–O–Si angles about the Si atom. This model has a much greater linear correlation to s-character and nuclear shielding than the previous models as shown in Figs. 2.9B and 2.10B respectively.

We further verify that this model has a reduced curvature compared to the $\langle \rho(\Omega_i) \rangle$ function over the sample space studied by employing techniques from vector calculus. The curvature of the sample surface may be analyzed by considering the curvature of the function at each point on the sample grid. The curvature of a line is defined as

$$\kappa = \left\| \frac{d\mathbf{T}}{ds} \right\| \tag{2.17}$$

where **T** is the unit tangent vector along a curve, s and the operator $||\mathbf{r}||$ represents the magnitude of a vector, **r**. For a vector function, **r(t)**, the curvature may be defined in an analytically more useful was as

$$\kappa = \frac{||\mathbf{r'(t)} \times \mathbf{r''(t)}||}{||\mathbf{r'(t)}||^3} \tag{2.18}$$

where **r'(t)** and **r"(t)** are the first and second derivatives of the unit tangent vector.

In order to analyze the curvature for Eqs. (2.12) and (2.16) in describing oxygen s-character, polynomials were fit to the data for each constant d_i. Attempting to describe the curvature of the surface using Eq. (2.18) would be far too unwieldy, so the curvature along the polynomial for each d_i was analyzed instead. To define the vector valued function of a polynomial fit to Eqs. (2.14) or (2.16) we obtain

$$\mathbf{r}\left(\Omega\right) = \left\langle \Omega, a_i f^2\left(\Omega\right) + b_i f\left(\Omega\right) + c_i \right\rangle \tag{2.19}$$

where f(Ω) may be either Eq. (2.12) or (2.16). For vector functions in the form of Eq. (2.19), Eq. (2.18) may be further simplified to

$$\kappa = \frac{|\boldsymbol{r}''(\Omega)|}{(1 + (\boldsymbol{r}'(\Omega))^2)^{3/2}}. \tag{2.20}$$

Substituting Eq. (2.19) in Eq. (2.20) results in

$$\kappa = \frac{\sqrt{(a_i f''^2(\Omega))^2 + (b_i f''(\Omega))^2}}{(1 + (af'^2(\Omega) + b_i f'(\Omega))^2)^{3/2}}. \tag{2.21}$$

The curvature along each polynomial of a given bond length for Eqs. (2.14) and (2.16) were then calculated using corresponding values for $a_i, b_i, f'(\Omega), f''(\Omega), f'^2(\Omega)$, and $f''^2(\Omega)$. The curvature for each function is shown in Fig. 2.12. It can be seen that the curvature of Eq. (2.16) is relatively constant and significantly lower than Eq. (2.12) over the entire sample space. Furthermore, Eq. (2.12) shows that curvature increases for increasing $\langle d_i \rangle$ and decreasing $\langle \Omega \rangle$.

Using the $\xi(\langle\Omega\rangle)$ function in place of the $\langle a_O^2 \rangle$ in Eq. (2.10) we obtain

$$\sigma_\xi(\langle\Omega\rangle, \langle d_i\rangle) = m_\xi(\langle d_i\rangle)\xi(\langle\Omega\rangle) + b_\xi(\langle d_i\rangle) \tag{2.22}$$

Next, $m_\xi(\langle d_i\rangle)$ and $b_\xi(\langle d_i\rangle)$ were fit to functional forms as was done for Eq. (2.11). As shown in Fig. 2.13, the slope $m(\langle d_i\rangle)$ is modeled using a linear functional form, whereas the intercept $b(\langle d_i\rangle)$

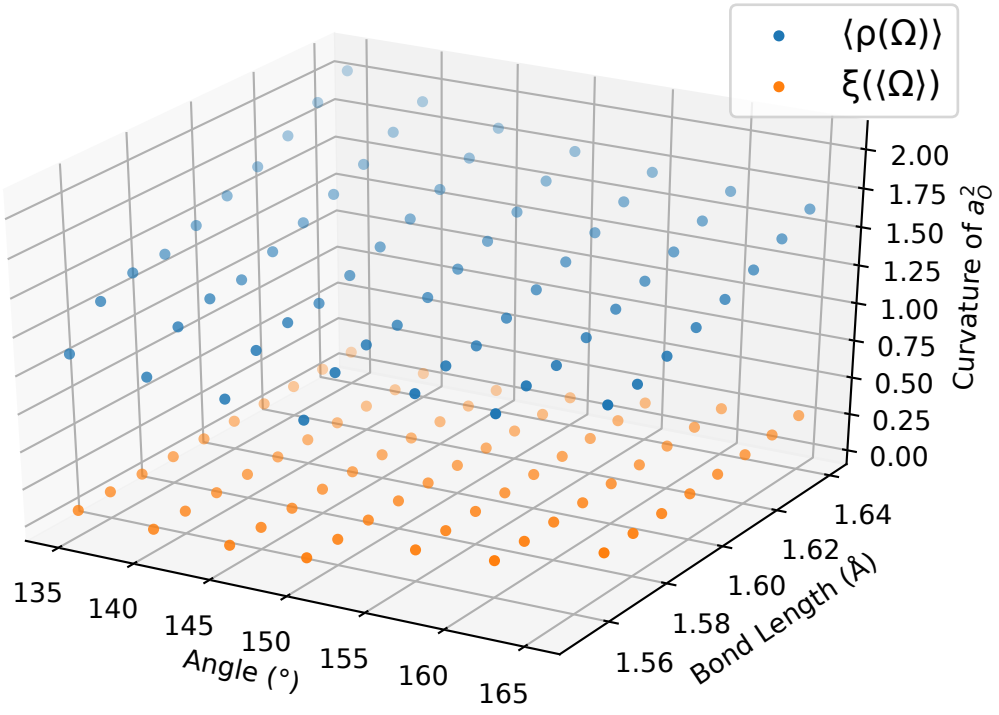

Figure 2.12: Curvature of the quadratic functions fit to $\langle \rho(\Omega) \rangle$ versus $\langle a_O^2 \rangle$ and $\xi(\langle \Omega \rangle)$ versus $\langle a_O^2 \rangle$ showing that $\xi(\langle \Omega \rangle)$ shows less curvature than $\langle \rho(\Omega) \rangle$ for the sample space.

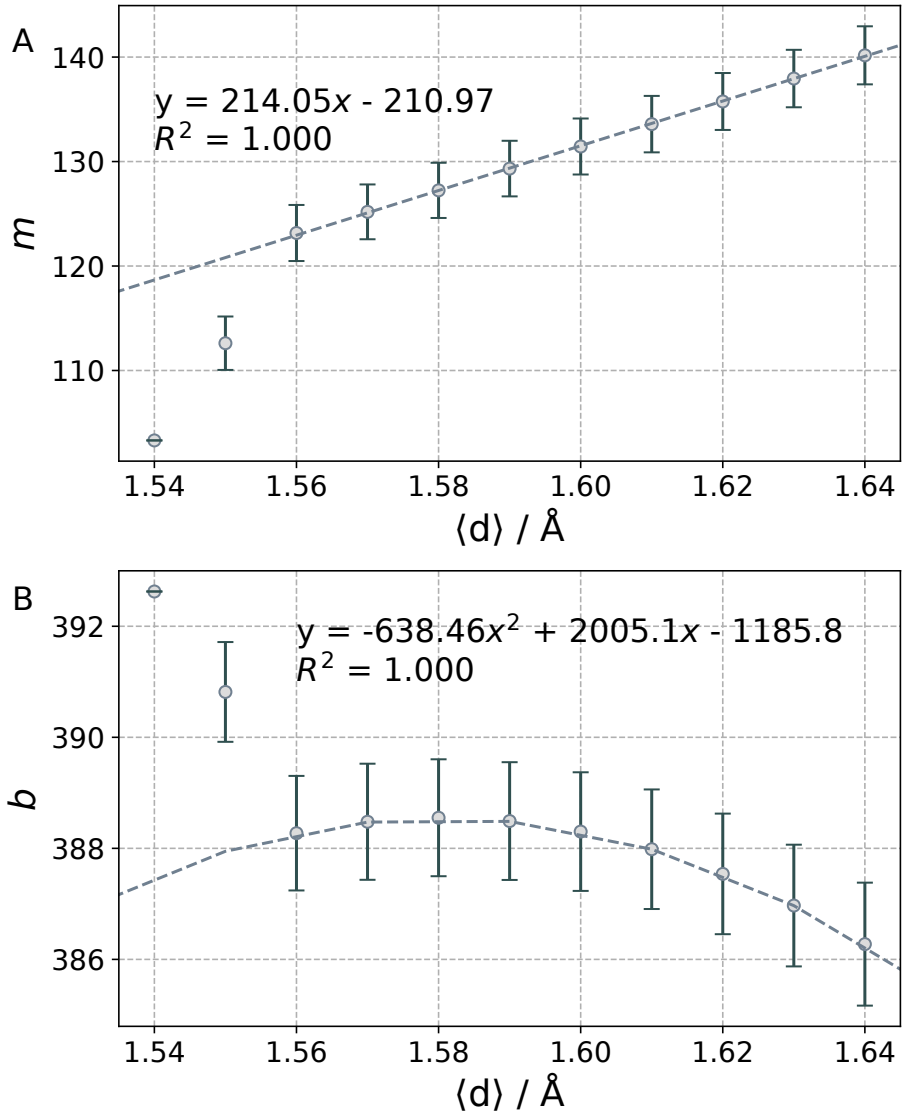

Figure 2.13: Bond distance versus (A) slope, m_i, showing a linear relationship and (B) intercept, b_i, showing a quadratic relationship.

is best modeled with a quadratic functional form. The points corresponding to $\langle d_i \rangle = 1.54$ Å and 1.55 Å were left out of consideration because the lack of points used to fit Eq. (2.22) for a constant bond distance skewed the fits from the expected behavior. Thus, the full proposed functional form is

$$\sigma(\langle \Omega \rangle, \langle d_i \rangle) = (\alpha_\xi \langle d_i \rangle + \beta_\xi)\, \xi(\langle \Omega \rangle) + \left(\gamma_\xi \langle d_i \rangle^2 + \epsilon_\xi \langle d_i \rangle + \zeta_\xi\right) \tag{2.23}$$

Using the coefficients determined from the fits of the functional forms of $m(\langle d_i \rangle)$ and $b(\langle d_i \rangle)$ in the full $\xi(\langle \Omega \rangle)$, the model shows a strong linear correlation with a RMSE of 0.82 ppm, as shown in Fig. 2.14A.

To improve the model, the coefficients, $\alpha_\xi,\ \beta_\xi,\ \gamma_\xi,\ \epsilon_\xi,$ to ζ_ξ, of Eq. (2.23) were then determined via least-squares minimization using the entire data set of series 1-3 cluster calculations. The resulting model had an RMSE of 0.75 ppm, and is shown in Fig. 2.14B. The Engelhardt and Radeglia model of Eq. (2.14) and the Davis model of Eq. (2.15) were both fit to the same cluster data using least-squares linear regression to compare to Eq. (2.23), as shown in Fig. 3.1. The Engelhardt and Radeglia model resulted in an RMSE of 1.80 ppm and the Davis *et al.* model resulted in an RMSE of 1.17 ppm. The $\xi(\langle \Omega \rangle)$ based model performs better than both $\langle \rho(\Omega_i) \rangle$ based models and does so using average angle and distance making the $\xi(\langle \Omega \rangle)$ model superior in terms of both accuracy and simplicity.

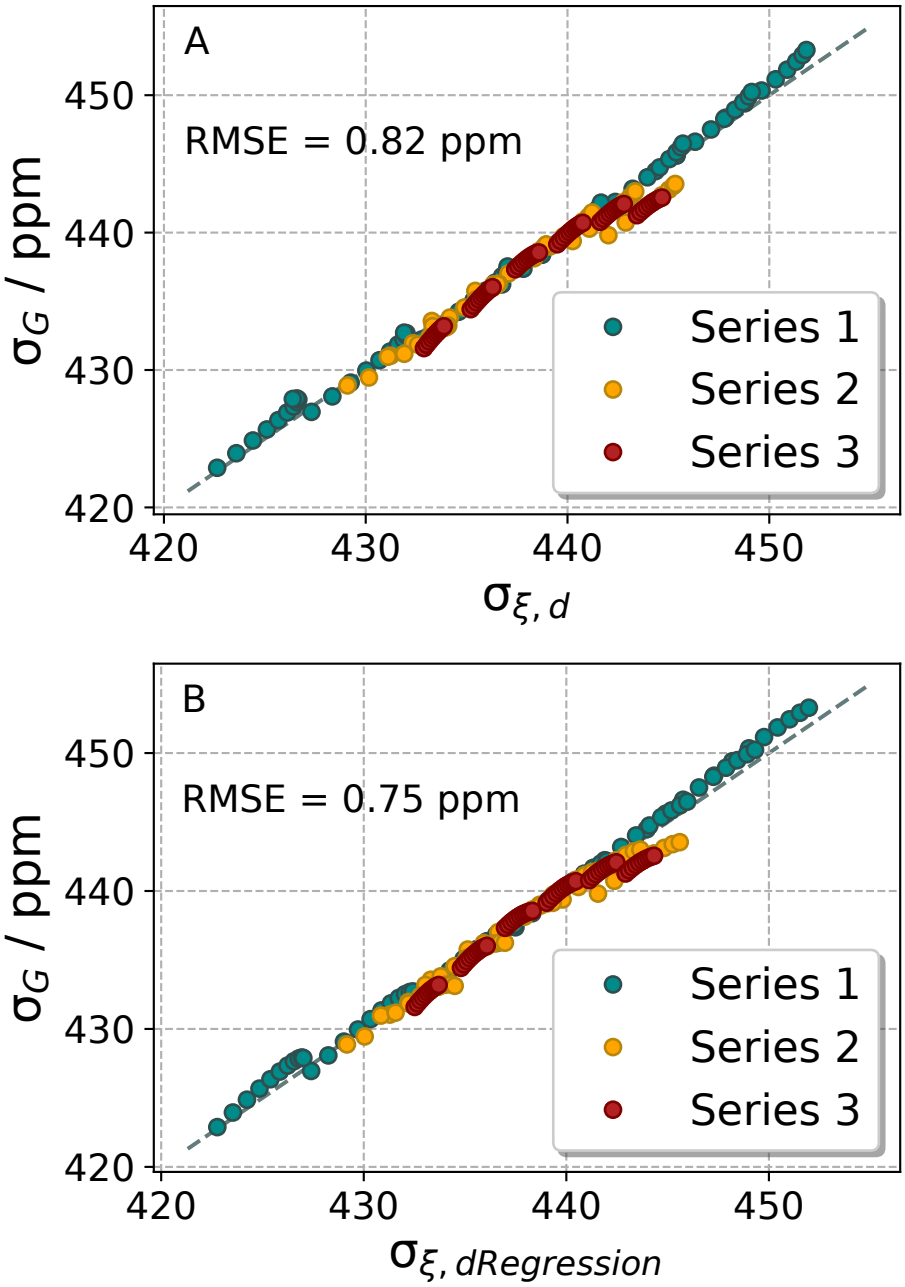

Figure 2.14: (A). Nuclear shielding predicted by the bond full ξ model using m_i and b_i coefficients determined from series 1 clusters. (B). Nuclear shielding predicted by the bond full ξ model using m_i and b_i coefficients determined via least squares minimization using series 1-3 clusters.

CHAPTER 3

Model Analysis

In its current state, Eq. (2.23) is difficult to use for NMR structural determination due to the difficulty in inverting the equation to solve for an average bond angle or average bond distance. Our next objective is to reduce the dimensionality of the model without significant loss in the performance of the model.

A principal component analysis reveals a high correlation of the variables in the full model, so *dimension reduction* techniques were used to simplify the full model without a significant loss of information. A PROMAX-rotated principal component analysis (PCA) using IBM SPSS 25 [25] was performed to reduce the dimensionality of the model. A PCA is a data transformation technique in which we reframe our data to better separate different components. In doing so, we order our components from most to least important which naturally allows us to reduce the dimensionality by removing the least important dimensions. The PCA technique allows us to see if the variables are correlated over the range of distances and angles chosen. If the variables are highly correlated then the removal of a variable is a possible method to reduce the dimensionality of the model.

3.1 Dimension Reduction

Principal Component Analysis

The following procedure for the PCA analysis is derived from Jackson's *A Users Guide to Principal Components* [26]. To perform a PCA, the data dimensions from Eq. (2.23), X, where

$$X = [d_i\xi, \xi, d_i^2, d_i]$$

Table 3.1: Correlation matrix of full ξ model, model 2.23.

		$(d_i\xi)'$	ξ'	$d_i'^2$	d_i'
Correlation	$(d_i\xi)'$	1.000	0.995	0.247	0.249
	ξ'	0.995	1.000	0.154	0.155
	$d_i'^2$	0.247	0.154	1.000	1.000
	d_i'	0.249	0.155	1.000	1.000

were converted to mean-adjusted data-dimension, X',

$$X' = [d_i\xi_i - \overline{d_i\xi}, \xi_i - \overline{\xi}, d^2_{\text{Si–O,i}} - \overline{d_i^2}, d_{\text{Si–O,i}} - \overline{d_i}] = [d_i\xi', \xi', d_i'^2, d_i']$$

by subtracting the mean of each data dimension from the respective data dimension creating a data set with the mean value centered about the origin.

Next, the correlations between each data dimension are calculated by

$$\text{corr}(X, Y) = \frac{\text{cov}(X, Y)}{s_X \; s_Y}, \tag{3.1}$$

where the $\text{cov}(X, Y)$ is the covariance of data dimensions X and Y and s is the standard deviation of a data dimension. The covariance is calculated as

$$\text{cov}(X, Y) = \frac{1}{n}\sum_{i=1}^{n}(x_i - E(X))(y_i - E(Y)), \tag{3.2}$$

where E(X) and E(Y) are the mean values of the data dimensions X and Y. The standard deviation is calculated as

$$s_x = \sqrt{\frac{\sum_{i=1}^{n}(x_i - E(X))^2}{n-1}}. \tag{3.3}$$

The correlations between each data dimension are summarized in table 3.1. These correlations were then used to construct a correlation matrix, P,

$$P = \begin{pmatrix} 1.000 & 0.995 & 0.247 & 0.249 \\ 0.995 & 1.000 & 0.154 & 0.155 \\ 0.247 & 0.154 & 1.000 & 1.000 \\ 0.249 & 0.155 & 1.000 & 1.000 \end{pmatrix}. \tag{3.4}$$

With a correlation matrix constructed, the principal components were determined by calculating the eigenvectors and eigenvalues of the correlation matrix. The eigenvalues and eigenvectors were solved from the eigenvalue problem

$$P\boldsymbol{v} = \lambda\boldsymbol{v} \Longrightarrow (P - \lambda I)\boldsymbol{v} = 0 \tag{3.5}$$

where λ represents the eigenvalues and $\boldsymbol{v}$ represents the corresponding eignevectors. The eigenvalues are found by finding the roots of the characteristic polynomial, $p(\lambda)$, given by

$$p(\lambda) = \det(P - \lambda I) \tag{3.6}$$

From the roots of $p(\lambda)$, an eigenvalue matrix, D, may be constructed as

$$D = (\lambda_1, \lambda_2, \lambda_3, \lambda_4)I = \begin{pmatrix} -0.0003 & 0 & 0 & 0 \\ 0 & 0.0008 & 0 & 0 \\ 0 & 0 & 1.5977 & 0 \\ 0 & 0 & 0 & 2.4018 \end{pmatrix}. \tag{3.7}$$

and the corresponding eigenvector matrix, V, may be constructed as

$$V = (\boldsymbol{v_1}, \boldsymbol{v_2}, \boldsymbol{v_3}, \boldsymbol{v_4}) = \begin{pmatrix} -0.3923 & 0.5956 & -0.4737 & 0.5167 \\ 0.3837 & -0.5846 & -0.5320 & 0.4775 \\ -0.5718 & -0.4172 & 0.4968 & 0.5022 \\ 0.6098 & 0.3598 & 0.4958 & 0.5028 \end{pmatrix} \tag{3.8}$$

At this point the data transformation from PCA is completed and we may now move on to dimension reduction. We have transformed our data from four variables to four components that maximize the variance that each component describes. As previously stated, the importance of the components is determined by the magnitude of the eigenvalues. Our eigenvalues in D are ordered from least important to most important, so we may naturally perform dimension reduction by removing the least important components and their corresponding eignevectors. A *feature vector*, F, was constructed from the two eigenvectors with the largest eigenvalues, where the first vector in F is from the most important eigenvector in V and the second vector in F is the second most important eigenvector in V,

$$F = \left(\begin{pmatrix} 0.5167 \\ 0.4775 \\ 0.5022 \\ 0.5028 \end{pmatrix}, \begin{pmatrix} -0.4737 \\ -0.5320 \\ 0.4968 \\ 0.4958 \end{pmatrix} \right),$$

Table 3.2: Component matrix of the principal component solution showing *loadings* of the original variables to each component.

	Component	
	1	2
$d_i\xi'$	0.801	0.599
ξ'	0.740	0.673
$d_i'^2$	0.778	-0.628
d_i'	0.779	-0.627

while the remaining eigenvectors may be removed to reduce the dimensionality at the expense of the information loss from the model. The two eigenvectors chosen as principal components are able to account for 99.995% of the variance of the observations.

The transformed data set is then produced from the product of the transpose of the feature vector and the transpose of the data dimensions

$$X'' = F^T \times X^T$$

Each principal component is represented as a linear combination of the original variables X'. The PCA is best interpreted using the *component loadings*, or the correlation coefficients between the variables with each component, where

$$r_{ij} = v_{ji}\sqrt{|d_i|}.$$

Here, v_{ji} is is an element of V and d_i is an element of D. These *loadings* show how well each component accounts for the original variables and shows relationships between the variables. There are two major groupings based on *component loadings*: $d_i\xi'$ and ξ' as one grouping and $d_i'^2$ and d_i' as the second grouping. Both groupings have high correlation with the first component, whereas the second component has positive correlation with the ξ grouping and negative correlation with the d_i grouping. From the two clusters of the component *loadings* the high correlation between the variables in each cluster indicate that the dimensionality of the original model may be reduced by dropping variables from each group.

Table 3.3: *Structure matrix* of PROMAX-rotated principal component solution.

	Component	
	1	2
$d_i'^2$	1.000	0.200
d_i'	1.000	0.201
ξ'	0.155	0.999
$d_i\xi'$	0.248	0.999

To obtain a structure matrix that is easier to interpret, a rotation of the axes about the origin may be performed. The rotation of axes is intended to maximize the *loadings* of variables onto each component axis to better reveal the structure of the component matrix, and show clustering of the variables. A PROMAX rotation procedure was performed which allows for an *oblique rotation* of the principal axes and relaxes the orthogonality constraint imposed by the PCA. In the oblique rotation, the component axes are reoriented to fall closer to the original variables and because the component axes no longer have an imposed orthogonality constraint, they may take any value. This results in an even simpler structure of the component matrix as *loadings* are maximized onto the component axes. The *loadings* of the original variables to the rotated component axes are shown in the *structure matrix* shown in Table 3.3.

The structure matrix more explicitly shows the clustering of the variables and further reveals the different components to be used in the models. From the structure matrix, d_i and d_i^2 have high *loadings* with the first component. If d_i increases so does d_i^2 and vice versa. Because both *load* with the first component, either may be used interchangeably as the first component. Furthermore, $d_i\xi(\langle\Omega\rangle)$ and $\xi(\langle\Omega\rangle)$ also have a high *loading* with component 2 and either may be used as component 2. From the different combinations of principal components, the following models were constructed based on Eq. (2.23):

$$\sigma_{3.9}(\langle\Omega\rangle, \langle d_i\rangle) = a_{3.9}\langle d_i\rangle\xi(\langle\Omega\rangle) + b_{3.9}\langle d_i\rangle^2 + c_{3.9} \tag{3.9}$$

$$\sigma_{3.10}(\langle\Omega\rangle, \langle d_i\rangle) = a_{3.10}\langle d_i\rangle\xi(\langle\Omega\rangle) + b_{3.10}\langle d_i\rangle + c_{3.10} \tag{3.10}$$

$$\sigma_{3.11}(\langle\Omega\rangle, \langle d_i\rangle) = a_{3.11}\xi(\langle\Omega\rangle) + b_{3.11}\langle d_i\rangle^2 + c_{3.11} \tag{3.11}$$

$$\sigma_{3.12}(\langle\Omega\rangle, \langle d_i\rangle) = a_{3.12}\xi(\langle\Omega\rangle) + b_{3.12}\langle d_i\rangle + c_{3.12} \tag{3.12}$$

3.2 Cross Validation with Computational Data

With four new dimension-reduced models, the best performing model must next be chosen. Using Python v3.7.3 [27] and scikit-learn library v0.21.0 [28], a 10-fold cross validation was performed to compare the performance of each model using an average RMSE across all folds as the performance metric. The cluster data from all three series was shuffled and partitioned into 10 folds with 9 of the folds retained as the training set and the remaining fold retained as the testing set. A linear regression line was fit to the training set and the regression line was used to predict the nuclear shieldings of the testing set. The RMSE was calculated for the testing set predicted values versus the observed values. This fitting and calculation of RMSE was repeated until every partition was used as a testing set. Furthermore, the entire process was repeated for an additional 99 cycles, shuffling the data each time, in an attempt to obtain coefficients of the regression fit converging to the optimal value. The average coefficients and RMSEs of each model are summarized below in Table 3.4:

From the results of the cross validation, it can be seen that each model, in terms of RMSE, has the same performance. This may also be seen when plotted, as shown in Fig. 3.2, in which each model shows the same behavior and they are nearly indistinguishable from each other. Additionally, it can be seen that the standard deviation in the coefficients is smaller for the $d_i\xi$ based models than the ξ based models and similarly the standard deviation is smaller when d_i^2 is used rather than d_i. In each case, however, the relative standard deviation is equivalent. As a result, all four

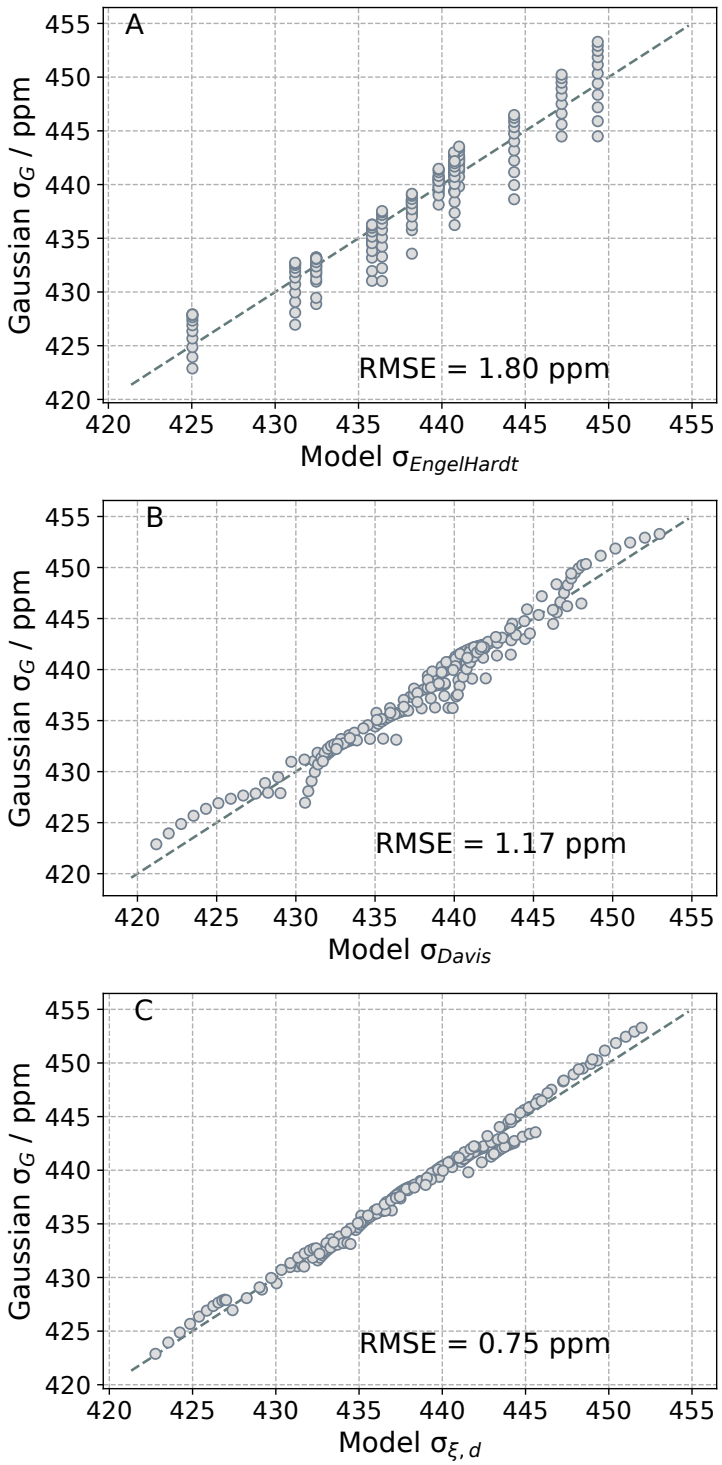

Figure 3.1: Gaussian calculated nuclear shielding versus model predicted nuclear shielding for A) Engelhardt and Radeglia, B) Davis *et al.*, and C) ξ models.

Model (i)	Variables	RMSE (ppm)	Coefficients (a_i, b_i, c_i)
3.9	$d_i\xi$, d_i^2	0.8 ± 0.1	$(80.7 \pm 0.3), (8.8 \pm 0.3), (365.7 \pm 0.7)$
3.10	$d_i\xi$, d_i	0.8 ± 0.1	$(80.7 \pm 0.3), (28.2 \pm 0.8), (343 \pm 1)$
3.11	ξ, d_i^2	0.8 ± 0.1	$(128.5 \pm 0.6), (18.6 \pm 0.3), (341 \pm 0.8)$
3.12	ξ, d_i	0.8 ± 0.1	$(128.5 \pm 0.6), (59.3 \pm 0.9), (293 \pm 1)$

Table 3.4: Average and standard deviation RMSE and coefficients calculated for PCA-reduced ξ models using 10-fold cross-validation of Gaussian cluster data.

models may be used, with no one model performing better than another. Furthermore, each model has very little increase in RMSE when compared to the total model with an RMSE of 0.75 ppm, indicating that the dimension reduction did not result in a significant loss of information.

3.3 Cross Validation With Experimental Data

The models developed in section 3.1 were further tested using experimental crystalline silica polymorph and single crystal zeolite data comprised of: tridymite, cristobalite, coesite, offretite, mordenite, chabazite, α-quartz, NaX, ZK-4, Sigma-2, Theta-1, ZSM-5, and ZSM-22. The sample set contained chemical shift and geometric data for 60 distinct Q^4 Si sites and is shown in Table 3.3.1.

3.3.1 Full Model Experimental Data Fitting

100 cycles of 10-fold cross-validation with shuffling between each cycle were performed on the full model as outlined in section 3.3 to determine the best coefficients for the model. The summary of the cross-validation is shown in Table 3.5. The model shows similar RMSE to the PCA-reduced models, however, the error in the coefficients is significantly larger in the full model. This is likely due to the fact that the variables have high correlation among each other, so a small change in one coefficient will have a change in a corresponding coefficient resulting in a difficulty in convergence. However, when the average coefficients are used in the model, shown in Fig. 3.3, the model is nearly indistinguishable from the PCA-reduced models, shown in Fig. 3.4.

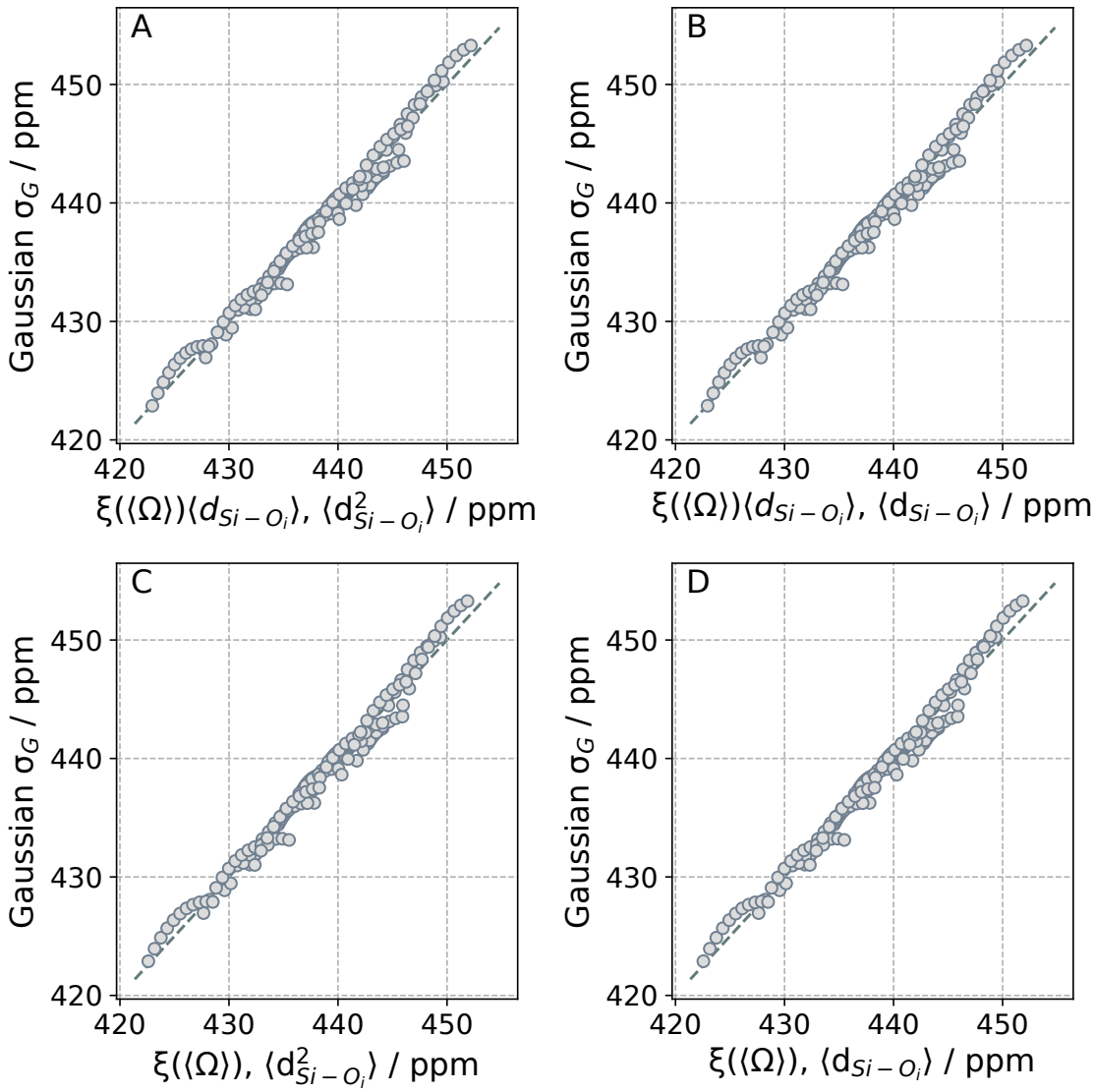

Figure 3.2: Nuclear shielding predicted by models A) 3.9, B) 3.10, C) 3.11, and D) 3.12 plotted against observed nuclear shielding using the coefficients in Table 3.4.

Model (i)	Variables	RMSE (ppm)	Coefficients (a_i, b_i, c_i)
2.23	$d_i\xi$, ξ, d_i^2, d_i	0.7 ± 0.3	$(125 \pm 180), (-308 \pm 290), (703 \pm 240),$ $(-2332 \pm 790), (1862 \pm 655)$

Table 3.5: Average and standard deviation RMSE and coefficients calculated for models 2.23 using 10-fold cross-validation of experimental crystalline data.

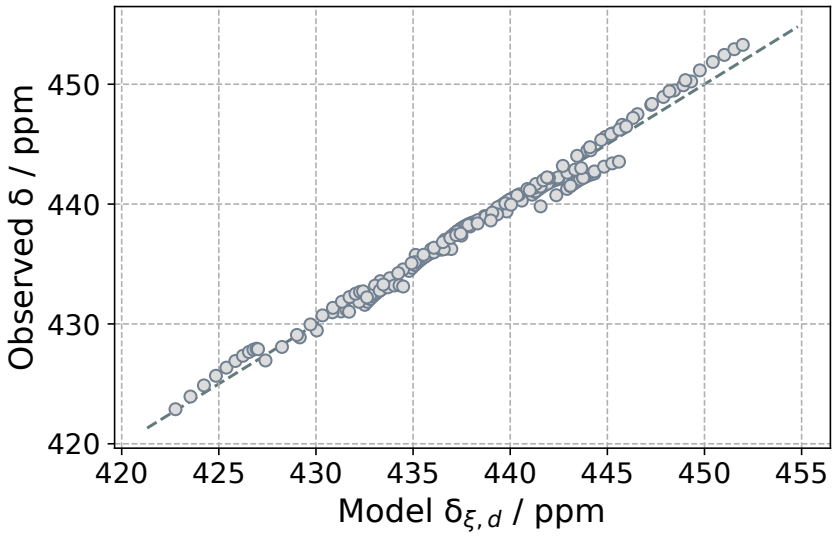

Figure 3.3: Resulting fit from 10-fold cross-validation of the full model, model 2.23.

	δ (ppm)	$\langle\Omega\rangle$	$\langle d_i\rangle$	ref.
Tridymite	-109.08	146.525	1.602	[6, 29]
	-109.14	146.7	1.598	
	-109.43	146.85	1.595	
	-110.36	148.125	1.6	
	-110.52	148.35	1.596	
	-110.8	148.425	1.595	
	-110.96	148.725	1.599	
	-111.09	149.075	1.606	
	-112.14	150.975	1.602	
	-113.16	151.8	1.599	
	-114.08	156.95	1.59	
	-114.33	157.175	1.585	
Cristobalite	-109.9	146.4	1.603	[6, 30]
Coesite	-108.1	143.4	1.612	[6, 31]
	-113.9	152.8	1.609	
Offretite	-107.2	142.5	1.651	[6, 32]
	-112.5	151.3	1.639	
Mordenite	-112.2	150.4	1.605	[6, 33]
	-113.1	152.3	1.605	
	-115.0	156.0	1.623	
Chabazite	-110.4	148.2	1.643	[6, 34]
Quartz	-107.4	143.6	1.61366	[6, 35]

Table 3.6: Crystalline silica polymorph chemical shifts, average Si–O–Si bond angles, and average Si–O bond distances.

Zeolite	δ (ppm)	$\langle\Omega\rangle$	$\langle d_i\rangle$	ref.
NaX	-103.4	139.2	1.619	[6, 36]
ZK-4	-110.5	148.3	1.622	[6, 37]
Sigma-2	-115.8	156.6	1.597	[3, 38]
	-113.6	151.1	1.599	
	-119.7	160.2	1.597	
	-108.5	146.7	1.600	
ZSM-5	-113.1	153.5	1.596	[38, 39]
	-113.1	153	1.591	
	-113.7	153	1.594	
	-113.7	152.7	1.599	
	-111.5	149.5	1.598	
	-113.9	155.4	1.596	
	-113.1	152.1	1.594	
	-116.8	158.8	1.589	
	-112.6	150.8	1.596	
	-111.8	150.4	1.597	
	-114.9	154.8	1.593	
	-113.7	153.9	1.592	
	-112.5	151.3	1.597	
	-115.7	155.6	1.595	
	-114.3	154.3	1.596	
	-115.8	156.9	1.597	
	-114.1	153.2	1.593	
	-113.7	152.1	1.598	
	-113.4	151.6	1.598	
	-113.1	153	1.596	
	-109.6	147	1.601	
	-112.3	151	1.597	
	-114.6	155	1.592	
	-113.7	153	1.591	
ZSM-22	-112.7	151.4	1.596	[40, 41]
	-113	153.2	1.589	
	-110.8	148.3	1.611	
	-114.3	153.2	1.603	
Theta-1	-112.7	149.3	1.589	[40, 42]
	-113	151.9	1.595	
	-110.9	149.4	1.586	
	-114.3	151.8	1.614	

Table 3.7: Siliceous zeolite chemical shifts, average Si–O–Si bond angles, and average Si–O bond distances.

Model (i)	Variables	RMSE (ppm)	Coefficients (a_i, b_i, c_i)
3.9	$d_i\xi$, d_i^2	0.6 ± 0.3	$(-66 \pm 1), (4.8 \pm 0.8), (-82 \pm 3)$
3.10	$d_i\xi$, d_i	0.6 ± 0.3	$(-66 \pm 1), (15 \pm 3), (-94 \pm 5)$
3.11	ξ, d_i^2	0.6 ± 0.3	$(-105 \pm 2), (-3.2 \pm 0.9), (-61 \pm 3)$
3.12	ξ, d_i	0.6 ± 0.3	$(-105 \pm 2), (-10 \pm 3), (-52 \pm 5)$

Table 3.8: Average and standard deviation RMSE and coefficients calculated for PCA-reduced ξ models using 10-fold cross-validation of experimental crystalline data.

3.3.2 PCA Reduced Model Fitting

The performance of the PCA reduced models was determined using 10-fold cross-validation as outlined in section 3.2. The results of the cross-validation are shown below in Table 3.8.

Similary to before with the cluster data, the cross-validation revealed that each model predicts the same RMSE. Again, the standard deviation in the coefficients shows the same trend seen with the cluster data, with the standard deviation in the coefficients for the $d_i\xi$ based models smaller than the ξ based models and, similarly, the standard deviation is smaller when d_i^2 is used rather than d_i. Again, this difference is minor and the relative standard deviation is approximately the same for the different variables across each model. Much like the model coefficients from the cluster data, when the predicted chemical shifts using the models with coefficients from Table 3.8 are plotted against observed chemical shifts the models are nearly indistinguishable from each other.

Because all of the dimension-reduced models perform the same with both *ab initio* and experimental crystal data, and all perform better as well as the full model, any model can be used to relate structural parameters to chemical shift. In order to determine the best, since performance was the same with each model, the focus is then shifted to simplicity of the model, and therefore, Eq. (3.12) is selected. Both Eqs. (3.11) and (3.12) performed well, giving approximately the same RMSEs in both the cluster and crystalline data. Eq. (3.12) is simpler, however, and is adopted.

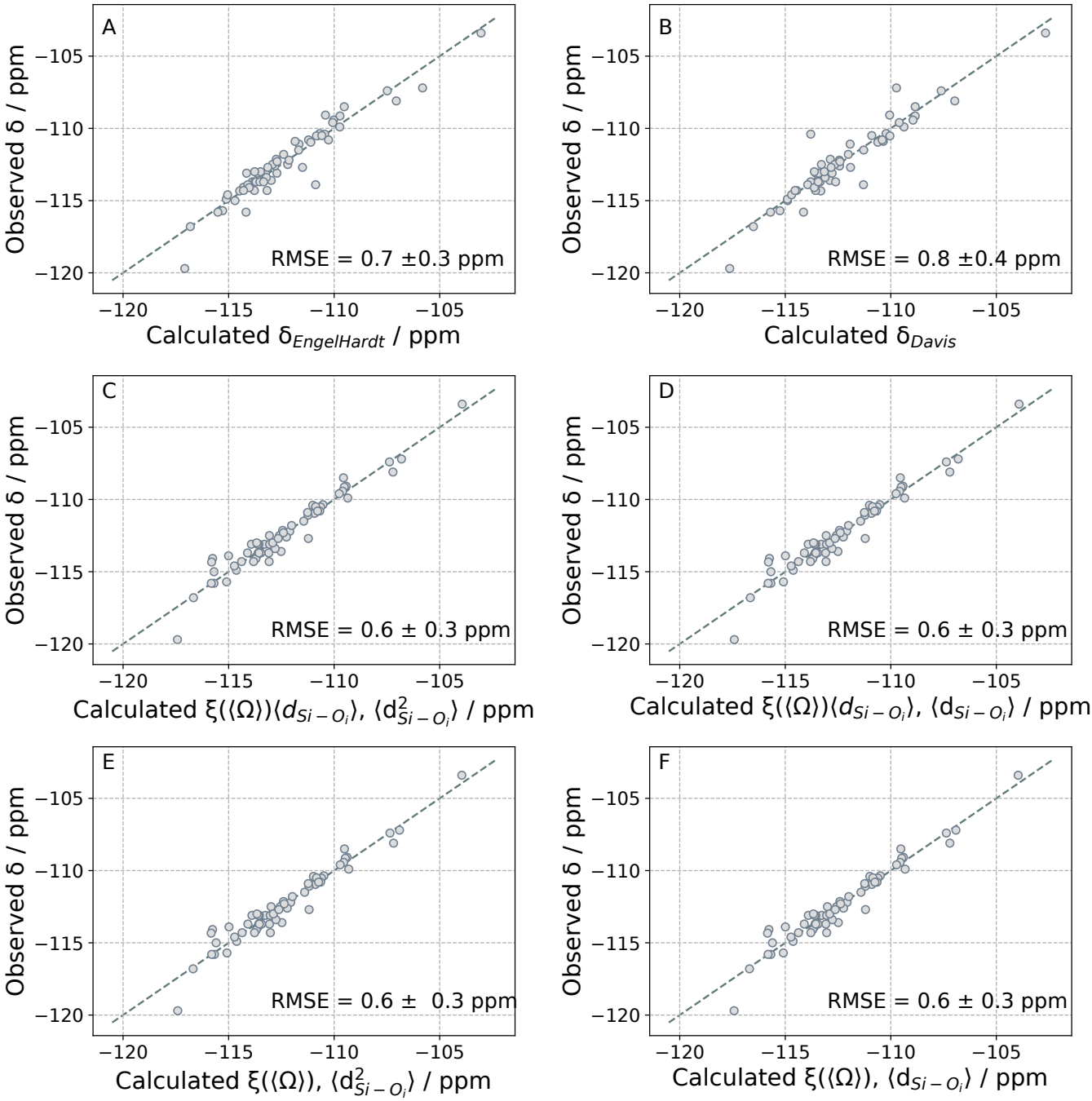

Figure 3.4: Chemical shifts predicted by the A) Engelhardt, B) Davis *et al.*, and C) full ξ model plotted against observed chemical shift using the coefficients in Table 3.8.

CHAPTER 4

First Attempts at NMR Crystallography and Future Directions for This Work

4.1 Sigma-2 Framework

From previous efforts, we have developed a model [4] for the $^2J_{\text{Si–O–Si}}$ couplings as a function of the double average Si–O–Si angle, $\langle\overline{\Omega}\rangle$, and the linkage Si–O–Si angle, Ω_0, given by

$$J(\Omega_0, \langle\overline{\Omega}\rangle) = -m_1\langle\overline{\Omega}\rangle \cos(\Omega_0)\left(\frac{\cos(\Omega_0)}{\cos(\Omega_0)-1}\right)^2 + J_0. \tag{4.1}$$

This model has been used to show the distributions of $\langle\overline{\Omega}\rangle$ and Ω_0 in vitreous silica to a much greater resolution than previous measurements using other techniques. Currently, we are interested in exploring the use of Eq. (4.1) with our chemical shift model, Eq. (3.12), in the structural refinement of siliceous zeolites.

Sigma-2 is used as an ideal candidate for testing refinement of crystal structures using ^{29}Si chemical shift data because the structure of Sigma-2 is accurately known from single crystal diffraction data [3, 38]. Using Eq. (4.1) we may calculate the expected $^2J_{\text{Si–O–Si}}$-couplings for Sigma-2 and a refined structure provided by Cadars *et al.* [3] and compare them to the observed values, as shown in Fig. 4.1. From the figure, it can be seen there is good agreement between the J-couplings calculated from Eq. (4.1) and the observed J-couplings from Table 2.1. There is, however, an outlier for both structures calculated to be 22.8 Hz versus the observed 20.5 Hz. The disparity of this single point despite the accuracy of the other points begs the question of why this point falls out of line. This point is from the J-coupling of Si1-Si3 linked through a bond angle of 172.4 °. From the expected distributions of Si–O–Si angles, an angle this high, while not impossible, is highly unlikely and may

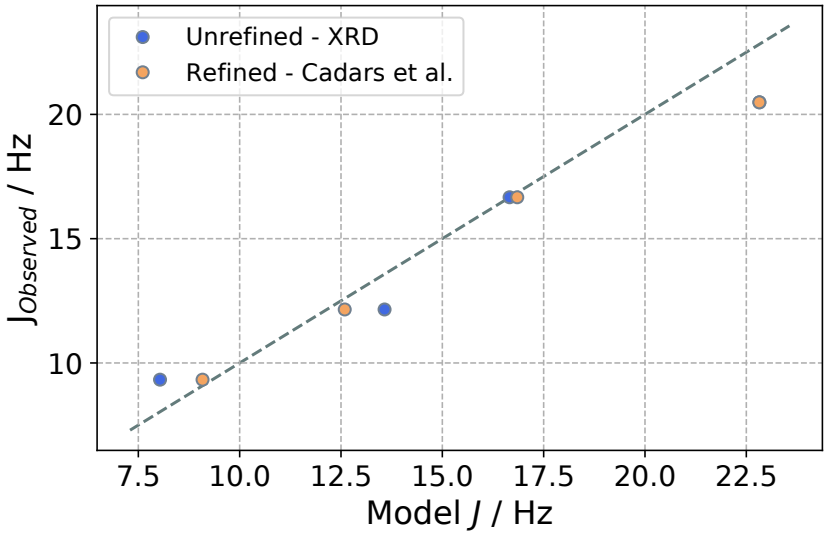

Figure 4.1: Calculated J-couplings for single crystal XRD-determined structure of Sigma-2 and a refined structure of Sigma-2 using Eq. (4.1 versus the observed J-couplings from an SE PIETA experiment in Fig. 2.2.

be an inaccurate angle measurement. Structural refinement using NMR interaction parameters is subject to the bias of whatever model is imposed on the structure. XRD measurements measure the mean atomic coordinates and distances from which the bond angles may be calculated. The high bond angle may be the result of error propagation through the calculated bond angle. Furthermore, Cadars *et al.* reported the Si1-Si3 J-coupling as 23.5 Hz which would be more in line with what is expected. Our findings using the SE PIETA sequence, however, show the J-coupling to be 20.5 Hz. Using the new and more accurate J-couplings would improve the structural refinement of Sigma-2. We believe that we may refine the structure to better reflect the Si–O–Si linkage angles as well as better match the observed NMR interaction parameters.

4.2 Structural Refinement of ZSM-12

The field of NMR crystallography has seen considerable efforts in the refinement of the crystal structures of materials that prove difficult to characterize. As previously stated, the crystal structures of many zeolites are often not accurately known due the difficulties in obtaining single crystals

for XRD analysis. These materials are of great commercial application and a better understanding of structure allows for better engineered zeolites. Previous refinement methods that have made use of *ab initio*-calculated ^{29}Si NMR interaction parameters have done so through the repeated process of adjusting atomic coordinates, calculating NMR parameters and comparing to experimentally observed NMR parameters [43]. NMR parameter calculations are time consuming and the repeated calculation over a unit cell is computationally expensive. Brouwer and colleagues [44, 45] have recently developed a simulated annealing algorithm which has been shown to use simple crystallographic measurements and atom connectivity as inputs to recreate zeolite structures with great agreement to experimental observations in a fraction of the time as *ab initio* based procedures. Brouwer and colleagues observed that in the determination of some zeolites they received multiple candidate structures with low cost functions from the algorithm. Brouwer and colleagues have also shown that comparing the *ab initio*-calculated NMR parameters to experimental NMR parameters is an accurate method to determine the best structure from the candidate structures. We believe, however, that using our J-coupling and chemical shift models would be more efficient and more applicable to a wider range of materials than *ab initio* methods.

From Fig. 4.2 it can be seen that there is an excellent agreement between the model and the observed ^{29}Si chemical shifts. There are, however, outliers as was seen in with the J-couplings in Fig 4.1. The outliers for the J-coupling was seen between Si1 and Si3 due to a rather large Si–O–Si linkage angle. With chemical shifts, we see that Si3, observed at -119.7 ppm, has a lower calculated chemical shift than expected, whereas Si1, observed at -115.8, is relatively accurate. The accuracy of Si1 is likely due to the fact that the high 172.8° angle is balanced out by a low 137.3° angle. Tossel *et al.* [22] found that the chemical shift relation to $\langle\Omega\rangle$ had very little variation and found there was very little difference in chemical shift if all bond angles were the same or if there were vastly different bond angles but a constant $\langle\Omega\rangle$. Si1, however, has 4 relatively high bond angles, resulting in an unlikely high $\langle\Omega\rangle$.

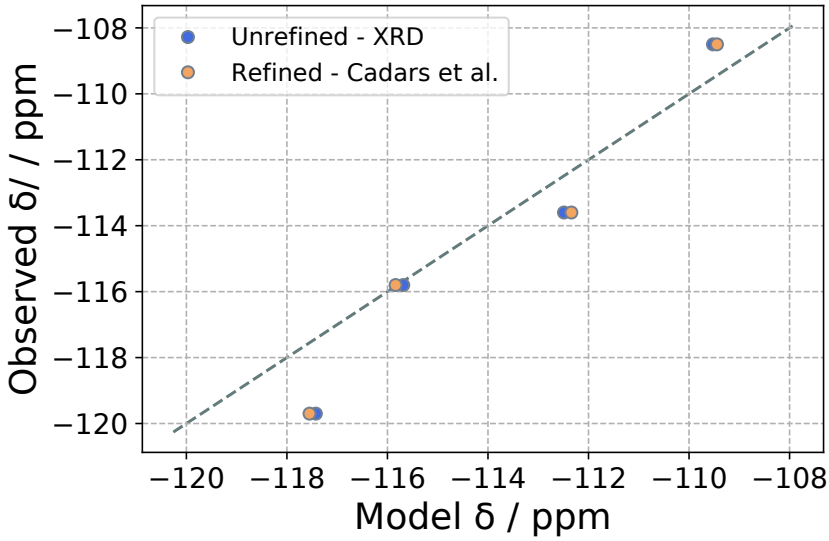

Figure 4.2: Calculated ^{29}Si chemical shifts crystal XRD-determined structure of Sigma-2 and a refined structure of Sigma-2 using Eq. (3.12) versus the observed ^{29}Si chemical shifts from an SE PIETA experiment in Fig. 2.2.

While we currently do not have a refinement procedure developed, it is worth using our models using crystal structures from current structure refinement attempts, namely that by Brouwer [43] and Chmelka *et al.* [3]. Both methods utilized DFT calculations of the chemical shift in their refinements where Brouwer utilized GIAO calculations and Chmelka *et al.* used CASTEP to also incorporate J-coupling into their refinement. We are calculating chemical shifts and J-couplings using refined and unrefined structure to verify that our models perform well and also to determine if both our models and the refined structures give good agreement to observed values. If both the models and the refinement procedures give better agreement to observed values then this is a promising sign that we may replace full *ab initio* calculations with our models and reduce computational complexity. The chemical shifts and J-couplings calculated from each crystal structure are shown compared to their observed values in Figs. 4.3 and 4.4 respectively.

Both the Brouwer and Chmelka methods improve the crystal structure in reproducing the chemical shift and J-coupling frequencies according to our models. Brouwer's refinement method performs better at minimizing the RMSE for the chemical shift, however, Chmelka *et al.* performs better in

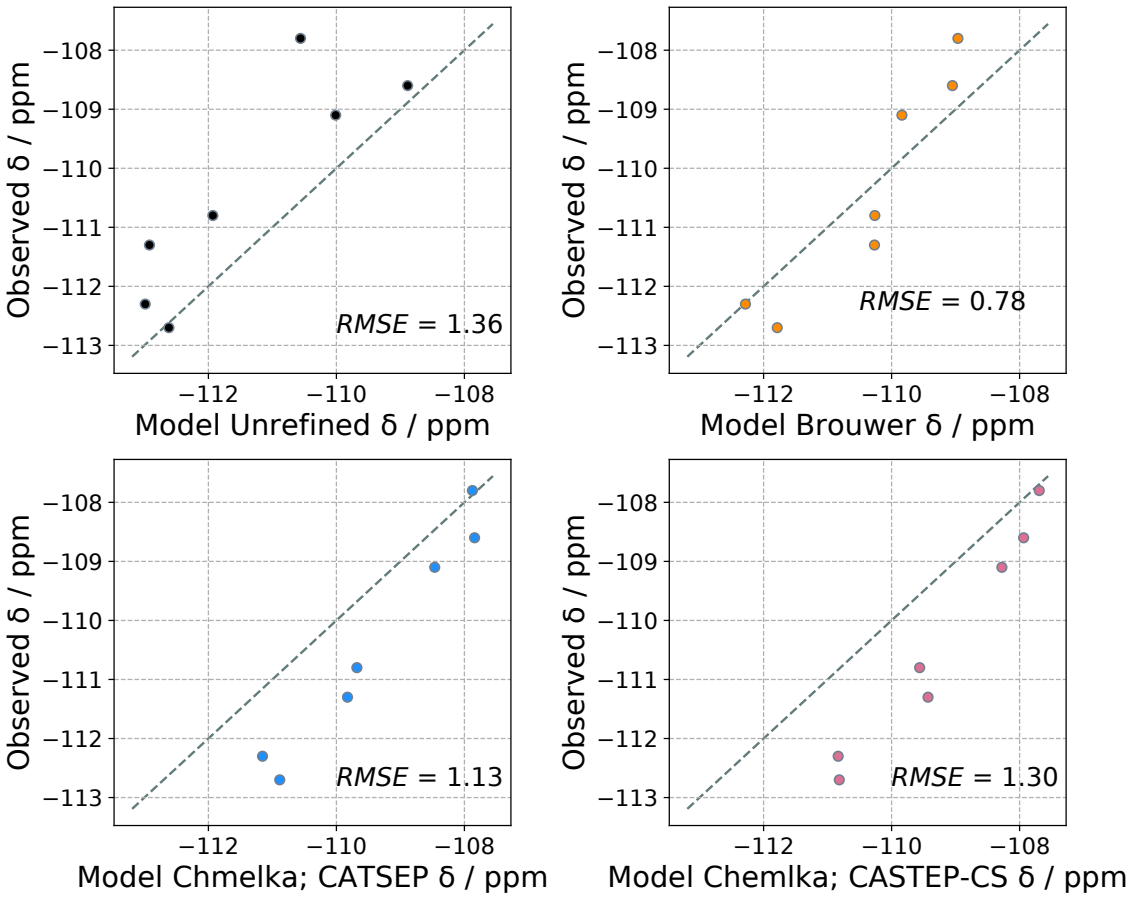

Figure 4.3: Experimentally observed chemical shifts versus those predicted by Eq. (3.12) using the ZSM-12 crsytal structure refinements by Brouwer and Chmelka *et al.*.

minimizing the RMSE for the couplings, however, only by a slightly greater amount than Brouwer. Although both refinement procedures reduced the spread of the data, ideally a refinement would reduce the RMSE from the calculations even more than Brouwer and Chmelka *et al.*.

Our models for chemical shift and J-coupling are promising as methods for refinement. In comparing the chemical shift dimensions versus the J-coupling dimension, as shown in Fig. 4.5, we can see a reasonable agreement between the observed values and the values calculated using the single crystal XRD measurements in Sigma-2. We are able to recreate the trends in the spectra shown in Fig. 2.2 with a reasonable accuracy, however, the comparison between the spectra and the calculated shows the limitations of our models. While we see a good agreement between most points

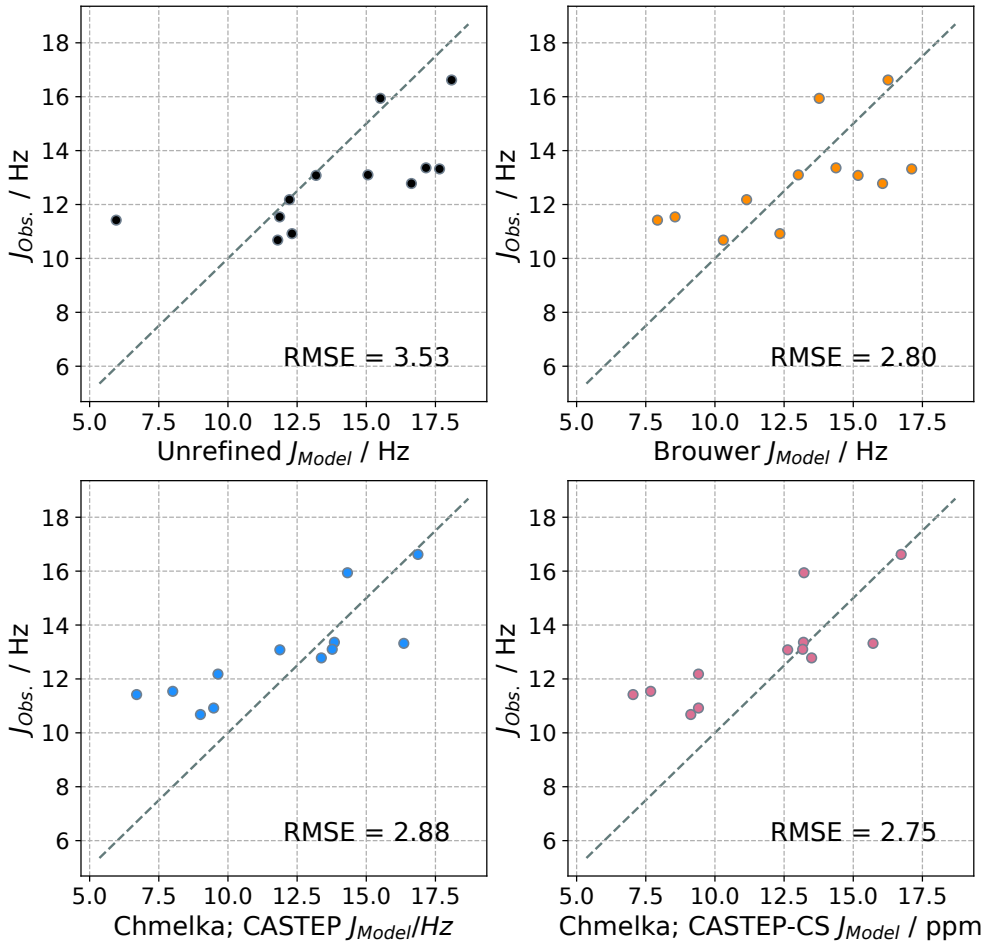

Figure 4.4: Experimentally observed chemical shifts versus those predicted by Eq. (4.1) using the ZSM-12 crsytal structure refinements by Brouwer and Chmelka *et al.*.

in our model, there are large deviations when the inter-tetrahedral angles are large. One potential flaw in our model is the lack of training data we have that contains these large angles. The majority of our data is concentrated in intermediate angles which places less emphasis on extreme angles when fitting our data. While our models may allow for an improvement in NMR crystallography by reducing computational time and also opening the doors to amorphous materials, we are also in need

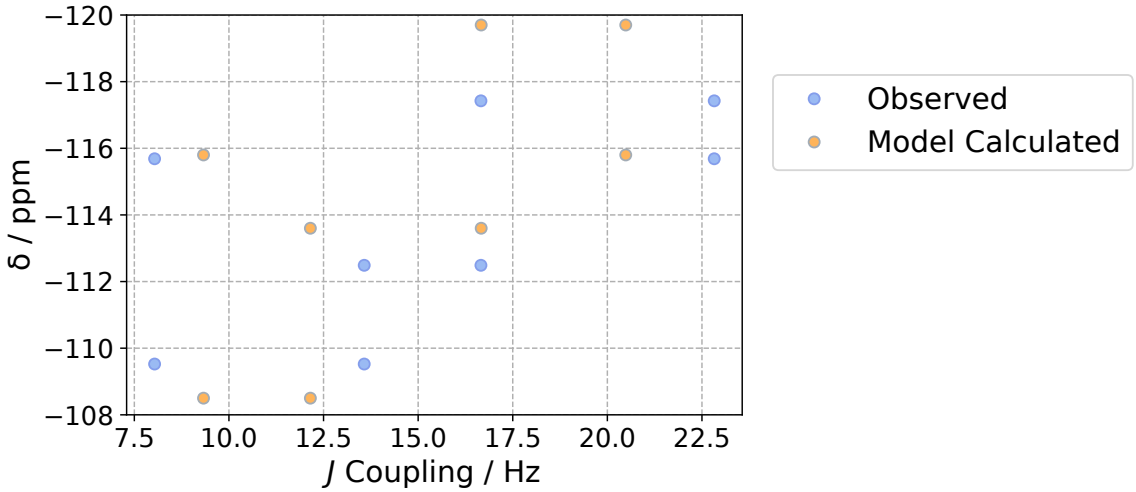

Figure 4.5: Experimentally observed chemical shift and J-couplings versus those predicted by Eq. (4.1) and Eq. (3.12) using the Sigma-2 crystal structure

of adequate training data to ensure that our models behave well over the range of experimentally observable angles and bond distances.

While we are able to recreate the spectra of Sigma-2 we must remember that this structure has single crystal XRD data available and so the structure is well known. The story changes, however, when we look at ZSM-12 where we only have powder diffraction measurements available, and thus do not know the structure very well. In plotting the chemical shift dimension against the J-coupling dimension, shown in Fig. 4.6, we can see a poor recreation of the spectra in Fig. 2.3. From our previous discussion on Sigma-2, we know that our models are able to return chemical shifts and J-couplings that agree with observed values when we use the structure parameters from the crystal structure. Therefore, we believe that we may adjust structure parameters in the crystal structure to better agree with the NMR parameters and in doing so, obtain a more accurate crystal structure than the powder diffraction structure.

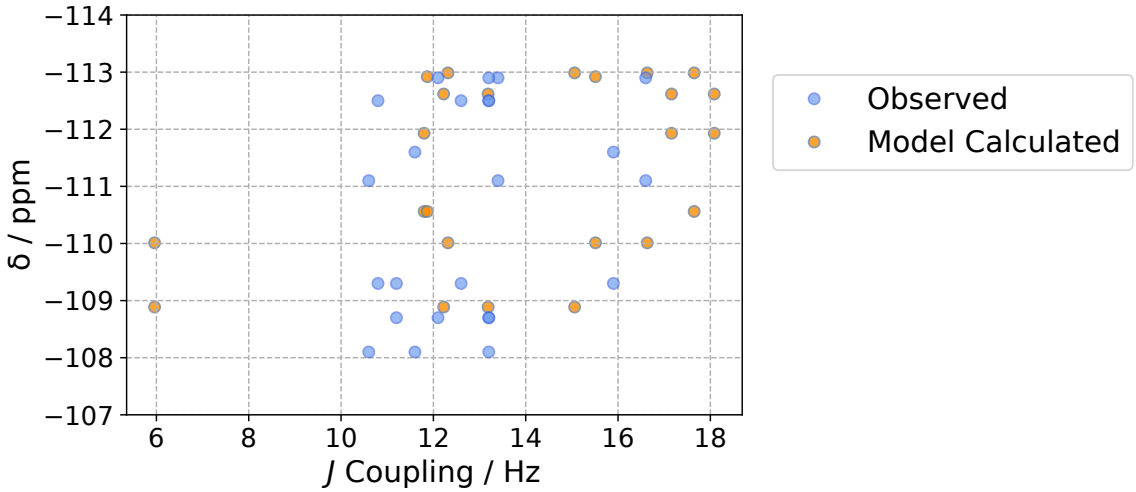

Figure 4.6: Experimentally observed chemical shift and J-couplings versus those predicted by Eq. (4.1) and Eq. (3.12) using the ZSM-12 crystal structure.

4.3 NMR Crystallography Summary

Current efforts in NMR crystallography typically involve the *ab initio* calculation of NMR parameters using quantum chemical software packages. Although these calculations have been able to produce relatively accurate NMR parameters [3] for silicate materials, we believe the calculations may not be the most efficient way to verify a structure through NMR. *Ab initio* calculations require a significant amount of computational resources and time. Calculating NMR parameters with quantum chemical software to refine a structure often takes hours to days on a supercomputer [43], whereas using a model such as Eq. (4.1) may take a fraction of that time per structure to calculate NMR parameters. Furthermore, *ab initio* calculations are impractical for structural determination and refinement of amorphous materials because there is no periodic unit in an amorphous material. The calculated NMR parameters of an aperiodic cell used in the calculations will fluctuate around the expected value and fail to converge except in the limit of an infinite cell, which is computationally impractical [46]. Our model-based approach, however, would remove the necessity of the full structure and could instead provide a distribution of the structural parameters in a material.

NMR interactions, such as J-couplings and chemical shift, are localized about an atom and there is very little effect from distant atoms beyond the first two coordination spheres. We believe that using a model developed to relate localized structure parameters, such as bond distances and bond angles, to NMR interaction parameters, like Eq. (4.1) and Eq. (3.12) is a time efficient and accurate alternative to an *ab initio* treatment of the refinement procedure.

BIBLIOGRAPHY

[1] S. Cadars, A. Lesage, N. Hedin, B. F. Chmelka, and L. Emsley, "Selective nmr measurements of homonuclear scalar couplings in isotopically enriched solids," *J. Phys. Chem. B*, vol. 110, pp. 16982 – 16991, Jan-08-2006 2006.

[2] P. Florian, F. Fayon, and D. Massiot, "$^{(2)}$J Si-O-Si scalar spin-spin coupling in the solid state: Crystalline and glassy wollastonite $CaSiO_3$," *J. Phys. Chem. C*, vol. 113, pp. 2562–2572, 2009.

[3] S. Cadars, D. H. Brouwer, and B. F. Chmelka, "Probing local structures of siliceous zeolite frameworks by solid-state NMR and first-principles calculations of ^{29}Si-O-^{29}Si scalar couplings," *Phys. Chem. Chem. Phys.*, vol. 11, pp. 1825–1837, 2009.

[4] D. J. Srivastava, P. Florian, J. H. Baltisberger, and P. J. Grandinetti, "Correlating geminal $^2J_{\text{Si–O–Si}}$ couplings to structure in framework silicates," *Phys. Chem. Chem. Phys.*, vol. 20, pp. 562 – 571, Jan-01-2018 2018.

[5] J. H. Baltisberger, B. J. Walder, E. G. Keeler, D. C. Kaseman, K. J. Sanders, and P. J. Grandinetti, "Phase incremented echo train acquisition in NMR spectroscopy," *J. Chem. Phys.*, vol. 136, pp. 211104–1–4, 2012.

[6] G. Engelhardt and R. Radeglia, "A semi-empirical quantum-chemical rationalization of the correlation between SiOSi angles and ^{29}Si NMR chemical shifts of silica polymorphs and framework aluminosilicates (zeolites)," *Chemical Physics Letters*, vol. 108, pp. 271 – 274, Jan-07-1984 1984.

[7] N. Janes and E. Oldfield, "Prediction of silicon-29 nuclear magnetic resonance chemical shifts using a group electronegativity approach: Applications to silicate and aluminosilicate structures," *J. Am. Chem. Soc.*, vol. 107, p. 6769, 1985.

[8] G. Engelhardt and D. Michel, *High-resolution solid-state NMR of silicates and zeolites*. Chichester: John Wiley & Sons, 1987.

[9] C. A. Fyfe, *Solid-State NMR for Chemists*. Guelph: C.F.C. Press, 1983.

[10] K. J. D. Mackenzie and M. E. Smith, *Multinuclear Solid-State NMR of Inorganic Materials*. Pergamon, 2002.

[11] M. M. Maricq and J. S. Waugh, "NMR in rotating solids," *J. Chem. Phys.*, vol. 70, p. 3300, 1979.

[12] P. J. Grandinetti, J. T. Ash, and N. M. Trease, "Symmetry pathways in solid-state NMR," *Prog. Nucl. Mag. Res. Sp.*, vol. 59, pp. 121–196, 2011.

[13] P. J. Grandinetti, J. H. Baltisberger, A. Llor, Y. K. Lee, U. Werner, M. A. Eastman, and A. Pines, "Pure absorption-mode lineshapes and sensitivity in two-dimensional dynamic angle spinning NMR," *J. Magn. Reson. A*, vol. 103, pp. 72–81, 1993.

[14] J. A. Aguilar, M. Nilsson, G. Bodenhausen, and G. A. Morris, "Spin echo nmr spectra without j modulation," *Chem. Commun.*, vol. 48, pp. 811 – 813, Jan-01-2012 2012.

[15] K. Takegoshi, K. Ogura, and K. Hikichi, "A perfect spin echo in a weakly homonuclear j-coupled two spin- system," *Journal of Magnetic Resonance (1969)*, vol. 84, pp. 611 – 615, Jan-10-1989 1989.

[16] P. C. van Zijl, C. T. Moonen, and M. von Kienlin, "Homonuclear j refocusing in echo spectroscopy," *Journal of Magnetic Resonance (1969)*, vol. 89, pp. 28 – 40, Jan-08-1990 1990.

[17] B. J. Walder, K. K. Dey, M. C. Davis, J. H. Baltisberger, and P. J. Grandinetti, "Two-dimensional NMR measurement and point dipole model prediction of paramagnetic shift tensors in solids," *J. Chem. Phys.*, vol. 142, p. 014201, 2015.

[18] M. J. Frisch, G. W. Trucks, H. B. Schlegel, G. E. Scuseria, M. A. Robb, J. R. Cheeseman, G. Scalmani, V. Barone, G. A. Petersson, H. Nakatsuji, X. Li, M. Caricato, A. V. Marenich, J. Bloino, B. G. Janesko, R. Gomperts, B. Mennucci, H. P. Hratchian, J. V. Ortiz, A. F. Izmaylov, J. L. Sonnenberg, D. Williams-Young, F. Ding, F. Lipparini, F. Egidi, J. Goings, B. Peng, A. Petrone, T. Henderson, D. Ranasinghe, V. G. Zakrzewski, J. Gao, N. Rega, G. Zheng, W. Liang, M. Hada, M. Ehara, K. Toyota, R. Fukuda, J. Hasegawa, M. Ishida, T. Nakajima, Y. Honda, O. Kitao, H. Nakai, T. Vreven, K. Throssell, J. J. A. Montgomery, J. E. Peralta, F. Ogliaro, M. J. Bearpark, J. J. Heyd, E. N. Brothers, K. N. Kudin, V. N. Staroverov, T. A. Keith, R. Kobayashi, J. Normand, K. Raghavachari, A. P. Rendell, J. C. Burant, S. S. Iyengar, J. Tomasi, M. Cossi, J. M. Millam, M. Klene, C. Adamo, R. Cammi, J. W. Ochterski, R. L. Martin, K. Morokuma, O. Farkas, J. B. Foresman, and D. J. Fox, "Gaussian 16 revision a.03," 2016.

[19] P. J. Stephens, F. J. Devlin, C. F. Chabalowski, and M. J. Frisch, "Ab initio calculation of vibrational absorption and circular dichroism spectra using density functional force fields," *The Journal of Physical Chemistry*, vol. 98, pp. 11623–11627, 1994.

[20] K. Wolinski, J. F. Hintou, and P. Pulay, "Efficient implementation of the gauge-independent atomic orbital method for NMR chemical shift calculations," *J. Am. Chem. Soc.*, vol. 112, pp. 8251–8260, 1990.

[21] E. D. Glendening, A. E. Reed, J. E. Carpenter, and F. Weinhold, "NBO Version 3.1."

[22] Y. Liu, H. Nekvasil, and J. A. Tossell, "Explaining the effects of t-o-t bond angles on nmr chemical shifts in aluminosilicates: A natural bonding orbital (nbo) and natural chemical shielding (ncs) analysis," *J. Phys. Chem. A*, vol. 109, 2005.

[23] D. W. J. Cruickshank, "The role of 3d-orbitals in π-bonds between (a) silicon, phosphorus, sulphur, or chlorine and (b) oxygen or nitrogen.," *J. Chem. Soc.*, vol. 1077, p. 5486, 1961.

[24] N. Janes and E. Oldfield, "Oxygen-17 NMR study of bonding in silicates: The d-orbital controversy," *J. Am. Chem. Soc.*, vol. 108, p. 5743, 1986.

[25] I. Corporation, "Ibm spss statistics for windows, version 25.0," 2017.

[26] J. E. Jackson, *A Users Guide to Principal Components*. John Wiley and Sons, Inc, 1991.

[27] P. S. Foundation, "Python language reference, version 3.7.3," 2019.

[28] F. Pedregosa, G. Varoquaux, A. Gramfort, V. Michel, B. Thirion, O. Grisel, M. Blondel, P. Prettenhofer, R. Weiss, V. Dubourg, J. Vanderplas, A. Passos, D. Cournapeau, M. Brucher, M. Perrot, and E. Duchesnay, "Scikit-learn: Machine learning in python," *Journal of Machine Learning Research*, vol. 12, p. 2825–2830, 2011.

[29] W. H. Baur, "Silicon–oxygen bond lengths, bridging angles Si–O–Si and synthetic low tridymite," *Acta Crystallographica Section B Structural Crystallography and Crystal Chemistry*, vol. 33, pp. 2615 – 2619, Jan-08-1977 1977.

[30] D. Peacor, "High-temperature single-crystal study of the cristobalite inversion," *Z. Krist.*, vol. 138, pp. 274–298, 1973.

[31] G. V. Gibbs, C. T. Prewitt, and K. J. Baldwin, "A study of the structural chemistry of coesite," *Zeitschrift für Kristallographie*, vol. 145, p. 108, 1977.

[32] J. A. Gard and J. M. Tait, "The crystal structure of the zeolite offretite, $k_1.1ca_1.1mg_0.7[si_12.8al_5.2o_36].15.2h_2o$," *Acta Crystallographica Section B*, vol. 28, pp. 825–834, 1972.

[33] J. Schlenker, J. Pluth, and J. Smith, "Positions of cations and molecules in zeolites with the mordenite framework ix dehydrated h-mordenite via acid exchange," *Materials Research Bulletin*, vol. 14, pp. 849 – 856, 1979.

[34] W. Mortier, J. Pluth, and J. Smith, "Positions of cations and molecules in zeolites with the chabazite framework. iv hydrated and dehydrated cu2+-exchanged chabazite," *Materials Research Bulletin*, vol. 12, pp. 1001 – 1007, 1977.

[35] Y. Le Page, L. Calvert, and E. Gabe, "Parameter variation in low-quartz between 94 and 298k," *Journal of Physics and Chemistry of Solids*, vol. 41, pp. 721–725, 12 1980.

[36] D. H. Olson, "Reinvestigation of the crystal structure of the zeolite hydrated nax," *The Journal of Physical Chemistry*, vol. 74, pp. 2758–2764, 1970.

[37] V. Gramlich and W. M. Meier, "The crystal structure of hydrated naa: A detailed refinement of a pseudosymmetric zeolite structure," *Zeitschrift fur Kristallographie - New Crystal Structures*, vol. 133, pp. 134–149, 1971.

[38] D. H. Brouwer, "NMR crystallography of zeolites: Refinement of an NMR-solved crystal structure using ab initio calculations of ^{29}Si chemical shift tensors," *J. Am. Chem. Soc.*, vol. 130, pp. 6306 – 6307, 2008.

[39] H. van Koningsveld, J. Jansen, and H. van Bekkum, "The monoclinic framework structure of zeolite h-zsm-5. comparison with the orthorhombic framework of as-synthesized zsm-5," *Zeolites*, vol. 10, pp. 235 – 242, 1990.

[40] C. A. Fyfe, G. T. Kokotailo, H. Strobl, C. S. Pasztor, G. Barlow, and S. Bradley, "Combined use of nuclear magnetic resonance, electron microscopy, and diffraction techniques as a probe of the uniqueness of zeolite structures: zeolites kz-2, theta1, zsm-22, and nu10," *Zeolites*, vol. 9, pp. 531–534, 11 1989.

[41] B. Marler, "Silica-zsm-22: synthesis and single crystal structure refinement," *Zeolites*, vol. 7, pp. 393 – 397, 1987.

[42] M. Z. Papiz, S. J. Andrews, A. M. Damas, M. M. Harding, and R. M. Highcock, "Structure of the zeolite theta-1. redetermination using single-crystal synchrotron-radiation data," *Acta Crystallographica Section C*, vol. 46, pp. 172–173, 1990.

[43] D. H. Brouwer, "A structure refinement strategy for NMR crystallography: An improved crystal structure of silica-zsm-12 zeolite from ^{29}Si chemical shift tensors," *J. Magn. Reson.*, vol. 194, pp. 136 – 146, 2008.

[44] M. H. D.H. Brouwer, "A simulated annealing approach for solving zeolite crystal structures from two-dimensional nmr correlation spectra," *Solid State Nuclear Magnetic Resonance*, vol. 65, pp. 89 – 98, 2015.

[45] D. Brouwer and J. V. Huizen, "Nmr crystallography of zeolites: How far can we go without diffraction data?," *Magnetic Resonance in Chemistry*, vol. 57, pp. 167–175, 2019.

[46] G. Makov and M. C. Payne, "Periodic boundary conditions in ab initio calculations," *Phys. Rev. B*, vol. 51, pp. 4014–4022, 1995.